

Advancing aortic stenosis assessment: validation of fluid-structure interaction models against 4D flow MRI data

Alberto Zingaro^{1,*}, Irmantas Burba^{1,*}, David Oks¹, Mauro Fontana¹, Cristóbal Samaniego², Micha Bischofberger³, Bart de Boeck⁴, Andre Douverny³, Özge Karakas³, Stefan Toggweiler⁴, Dabit Arzamendi-Aizpurua^{5, 6}, Utku Gülan³, and Mariano Vázquez^{1, 2}

¹ELEM BioTech, Pier 07, Calle Laietana, 26, Barcelona, 08003, Spain

²Barcelona Supercomputing Center, Plaça d'Eusebi Güell, 1-3, Barcelona, 08034, Spain

³Hi-D Imaging, Technoparkstrasse 2, Winterthur, 8406, Switzerland

⁴Lucerne Cantonal Hospital (Luzerner Kantonsspital), Spitalstrasse, Luzern, 6000, Switzerland

⁵Cardiology Department, Hospital de la Santa Creu i Sant Pau., Carrer St. Antoni M. Claret 89, Barcelona, 08025, Spain

⁶Department of Medicine, Universitat Autònoma de Barcelona, Pg. Vall d'Hebron, 119-129. , Barcelona, 08023, Spain

*These authors equally contributed to this work

Abstract

Systematic *in vivo* validations of computational models of the aortic valve remain scarce, despite successful validation against *in vitro* data. Utilizing a combination of computed tomography and 4D flow magnetic resonance imaging data, we developed patient-specific fluid-structure interaction models of the aortic valve immersed in the aorta for five patients in the pre-transcatheter aortic valve replacement configuration. Incorporating also an *in vitro* setup of the valve, our computational models are subjected to rigorous validation against 4D flow measurements. Our results demonstrate the models' capacity to accurately replicate flow dynamics within established ranges of uncertainties mainly arising from 4D flow noise. In addition, we illustrate how computational models can serve as valuable cross-checks to reduce noise and erratic behaviour of *in vivo* data. This study represents a significant step towards integrating *in silico* technologies into real clinical contexts, providing a robust framework for improving aortic stenosis diagnosis and the design of next-generation aortic valve bioprostheses.

Keywords: Aortic Valve, Aortic Stenosis, TAVR, Cardiac Modeling, Fluid-Structure Interaction, Finite Element Method, Validation, In-vivo, 4DFlow MRI

1 Introduction

Aortic Stenosis (AS) represents a constriction of the Aortic Valve (AV) opening and stands as the most prevalent valvular pathology in developed nations, affecting 9 million people globally. Left

untreated, it dramatically increases the risk of sudden cardiac death and heart failure [1, 2] with a one-year mortality rate as high as 50%. Transcatheter Aortic Valve Replacement (TAVR) addresses AS by replacing a dysfunctional or diseased AV with a prosthetic valve made from animal pericardial tissue [3]. Distinguished from conventional methods like Surgical Aortic Valve Replacement, TAVR emerges as a minimally invasive alternative, offering distinct advantages for patients [4, 5]. The severity of AS and the outcomes of TAVR are typically gauged using various Quantities of Interest (QoIs) such as Aortic Valve Area (AVA), Transvalvular Pressure Gradient (TPG), peak transvalvular velocity, velocity ratio, and Left Ventricle Outflow Track (LVOT) diameter. These QoIs are routinely assessed using imaging techniques such as doppler echocardiography, Cardiac Magnetic Resonance (CMR), Computed Tomography (CT) angiography, or more advanced techniques such as 4D flow Magnetic Resonance Imaging (MRI). [6, 7, 8, 9]. However, these techniques have limitations. The reliability of the assessment is intricately tied to the operator’s experience and expertise, thereby introducing potential variability [10]. Furthermore, challenges arise in effectively visualizing specific flow structures – particularly in scenarios involving eccentric jets and turbulent flows – thereby contributing to suboptimal image quality and errors in velocity measurements [10, 11]. Additionally, in cases of low ejection fraction, further limitations may be encountered, potentially complicating the interpretation of results and accuracy of assessments. Advanced techniques like 4D flow MRI, despite their ability to visualize the velocity field, are predominantly limited to research applications rather than being integrated into clinical routine. Additionally, the computation of certain QoIs (such as the AVA) relies on formulas based on several hypotheses about blood flow [12]. Consequently, both random and systematic measurement errors may potentially impact AS assessment, possibly leading to misdiagnosis and subsequent mistreatment with TAVR [13]. The precision of estimating these QoIs can be heightened by complementing these imaging techniques with *in silico* technologies, including Computational Fluid Dynamics (CFD) and Fluid Structure Interaction (FSI) AV models. The latter specifically entails the interaction between blood hemodynamics and the mechanical behavior of the AV, providing the computations of several QoIs useful in the context of AS risk prediction and TAVR assessment [14, 15, 16, 17, 18, 19, 20, 21, 22, 23, 24].

A wealth of literature exists on mathematical models of cardiac valves and their interaction with cardiac hemodynamics [25, 21, 26, 27, 28, 29, 30, 31, 32, 33, 34, 24, 35, 36, 37] and for a comprehensive review of FSI models for the blood-AV, we refer to the recent paper by Kuchumov et al. [38]. However, for *credibility evidence* in computational modeling for medical devices submission, different Verification, Validation, and Uncertainty Quantification (VVUQ) activities should be carried out, including validation processes against *in vitro* and *in vivo* datasets [39]. Several studies have presented computational FSI models of the blood-AV system conducting validation against *in vitro* data. *In vitro* flow measurements have been utilized to extract hemodynamics parameters in anatomically accurate silicone models and to validate numerical models in the literature [40, 41, 42]. Dumont et al. carried out a validation study of the blood-AV FSI in a 2D configuration against *in vitro* data [43]. Luraghi et al. compared FSI and structural mechanics simulations of polymeric heart valves against *in vitro* data, showing the capability of FSI in the replication of different patterns of the experiments [44]. In 2018, Tango et al presented a 3D validation study aimed at replicating an *in vitro* Particle Image Velocimetry (PIV) setup of the AV [45]. Sodhani et al. carried out a validation study against *in vitro* data for an artificial textile reinforced AV [46]. In the context of TAVR, Borowski et al. [47] validated an FSI model against PIV data. Thus, the literature on FSI models of AV dynamics is extensive, showcasing the robust theoretical foundation of these computational models.

Furthermore, during the past years – in line with the *credibility evidence* activities pointed out

by the Food and Drug Administration (FDA) and other regulatory agencies – particular attention has been devoted to the validation of these computational models, always in the context of replicating experimental setup. However, it is noteworthy that none of these models have undergone systematic validation against *in vivo* data, which somewhat still constrains their application in real clinical contexts. Indeed, the validation of computational models in cardiovascular applications against *in vivo* data poses a formidable challenge. This challenge arises primarily from the limited availability of data crucial for configuring boundary conditions and selecting specific model parameters (such as in the constitutive law for valve mechanics). Additionally, medical data often come with substantial noise and error, and their precision frequently hinges on the expertise of the individuals acquiring these measurements. This further complicates the process of data assimilation in the computational model and renders it challenging to assess the accuracy of numerical results in comparison to these inherently noisy *in vivo* datasets. This gap in the literature underscores an urgent need for the validation of FSI models of the AV against *in vivo* datasets.

The aim of this paper is to present a pipeline for the validation of FSI computational model of the AV against *in vivo* measurements. Utilizing a combination of CT and 4D flow MRI data, we build a computational model representing the AV immersed in the aorta for five patients in the pre-TAVR configuration (i.e. prior to TAVR procedure). Our computational model employs the Immersed Boundary (IB) method [48, 27] for FSI, as we recently proposed in [24], and undergoes validation against 4D flow MRI measurements. We establish the credibility of our model through a comprehensive comparison of various indicators and flow patterns. We demonstrate the computational model’s ability to accurately replicate flow dynamics, both qualitatively and quantitatively. Additionally, we demonstrate how our FSI computational model serves as a cross-check to mitigate noise and erratic behaviour in *in vivo* data. We discuss the pivotal role of numerical models and simulations in the context of AS, serving as tools capable of overcoming some of the limitations associated with current *in vivo* assessment, and enabling a more comprehensive understanding of complex physiological phenomena as AV dynamics. To the best of our knowledge, this is the first work that validates FSI computational models of the AV against *in vivo* data for several patients, marking a significant advancement in the integration of *in silico* technologies in real clinical contexts.

This paper is organized as follows: Section 2 introduces patient-specific data, the pipeline we developed to process them, our computational model and the validation data from 4D flow MRI acquisitions. In Section 3, we present our computational results against the *in vivo* dataset and additional QoIs that can be computed with FSI simulations. Section 4 is devoted to the discussion and we present limitations and conclusions in Section 5 and Section 6, respectively.

2 Methods

We present the methodology of the work. In Section 2.1 we introduce the patients cohort. Section 2.2 is focused on the postprocessing of CT and 4D flow MRI data. In Section 2.3, we introduced the *in vitro* setup from which we get the AV geometry. In Section 2.4, we show the computational model and its setup, whereas we explain how we feed the model with the *in vivo* flowrate in Section 2.5. In Section 2.6 we present a calibration study aimed at selecting the valve’s Young modulus.

	P1	P2	P3	P4	P5
age	81	77	89	74	66
sex	M	M	F	F	M
height [cm]	182	169	155	157	175
weight [kg]	78	64	56	46	130
annulus area [mm ²]	543	530	344	454	405
annulus perimeter [mm]	83	83	66	77	72
T_{HB} [s]	1.02	1.06	0.72	0.71	0.78

Table 1: Patients information. T_{HB} is the heartbeat period.

2.1 Patients selection

We consider clinical data belonging to the TURBULENT TAVI study¹, aiming to provide a better understanding of the intensity of turbulence in the ascending aorta before and after TAVR. The study hypothesizes that there is a correlation between *in vitro* and *in vivo* measurements. In the scope of the study, pre-TAVR and post-TAVR scans for patients undergoing TAVR at Heart Center Luzern, Switzerland were performed. In this paper, we consider five patients characterized by the same level of AS severity, namely P1, P2, P3, P4, and P5. Patient information is provided in Table 1. For these patients, we have available CT and 4D flow MRI acquisitions.

2.2 CT and 4D flow MRI post-processing

CT data are used to generate the volumetric fluid mesh, whereas 4D flow MRI is used for both data assimilation (in terms of input blood flowrate) and as a validation set (in terms of the whole velocity field and additional QoIs).

The CT data We segmented the aorta of the five patients using 3D Slicer [49], with particular emphasis on cleaning the leaflets region. Then, we perform some preprocessing steps to get the final mesh, as we show in Figure 1. These include a clipping of the original aortic geometry to include only the ascending portion of the aorta. Moreover, we remove the coronary arteries and we add flow extensions to both inlet and outlet sections. This is done to allow the fluid to fully develop as it enters, and to avoid potential instabilities at the outlet section.

The preprocessing of all the geometries and the creation of the meshes is carried out with the preprocessing software ANSA [50]. We generate tetrahedral meshes of the aorta, as we showcase in Figure 2 (left). Notice that, for the FSI model to properly capture the AV, we conveniently refine the fluid mesh in a region closer to the valve. Details of the generated meshes are provided in Table 2 (top).

The 4D flow MRI data In vivo free-breathing 4D-MRI measurements were performed with a 1.5 T scanner (Siemens Magnetom Aera, Siemens AG, Munich, Germany) to extract the velocity field phase-averaged over subsequent cardiac cycles: $\langle \mathbf{u}^{4\text{Dflow}}(\mathbf{x}, t) \rangle$. The imaging parameters were the following: spatial resolution $2.5 \times 2.5 \times 2.5 \text{ mm}^3$, field of view $250 \times 160 \times 50 \text{ mm}^3$, TR/TE 5, 8/3,

¹“Correlation between bench and clinical turbulent and mean kinetic energy after transcatheter aortic valve Implantation of the Allegra valve: the TURBULENT TAVI pilot study”, Luzerner Kantonsspital, Luzern, PI: PD Dr. med. Stefan Toggweiler, project ID 2019-01344

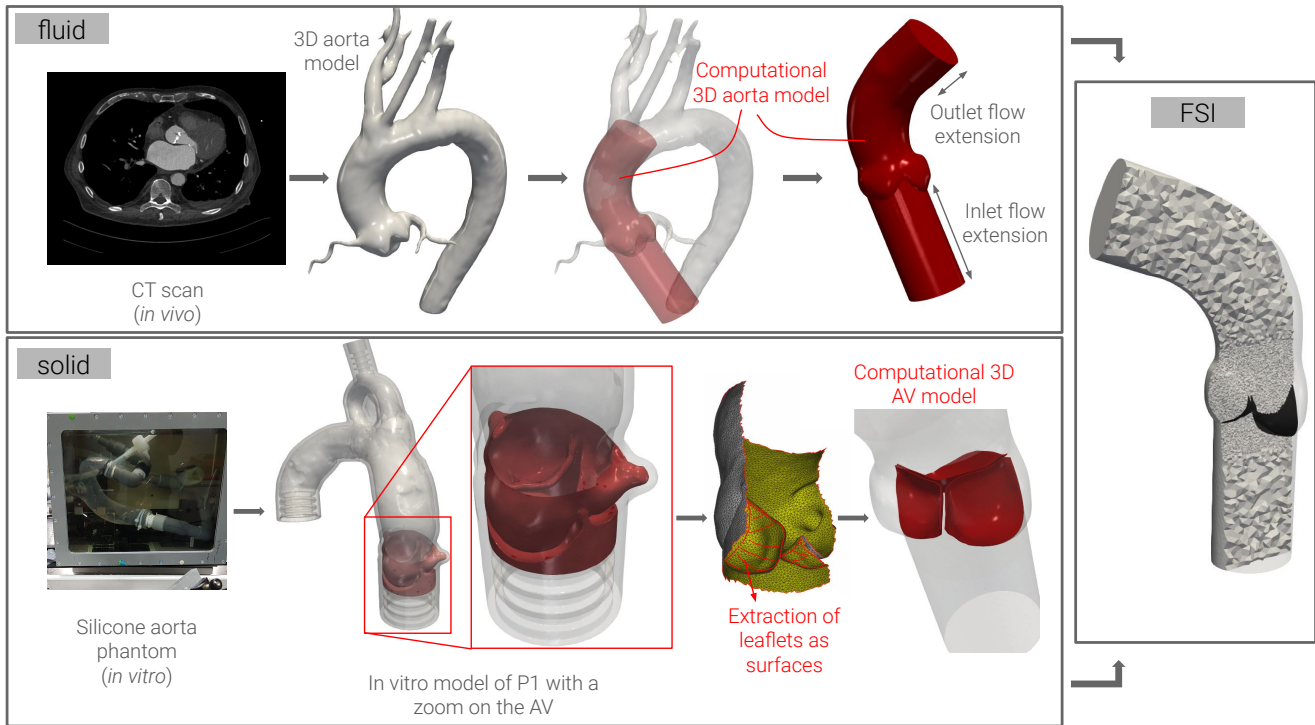


Figure 1: Preprocessing pipeline to generate the FSI meshes. Top: pipeline for the aorta: *in vivo* CT scan acquisition of the aorta, 3D segmented aorta, coronary arteries clipping and flow extensions adding to get the final computational domain. Bottom: preprocessing pipeline to generate our template AV mesh from the *in vitro* experiment of P1.

4 ms, and temporal resolution 35 ms. The velocity encoding values were 40, 100, and 200 cm s^{-1} per direction. The phase contrast sequences were synchronized with the electrocardiography. A 3D-gradient echo phase contrast sequence with multi-point velocity encoding was applied to obtain $10 \times k - t$ undersampled data. We give a graphical representation of the 4D flow MRI data in Figure 3. We use the 4D flow MRI for data assimilation and as a validation set. Specifically, the *in vivo* flowrate serves as our input flowrate, whereas several quantities are used to validate our computational results. We better detail both processes in Section 2.5 and Section 3.

2.3 In vitro setup

To construct the computational AV model, we leverage an *in vitro* setup meticulously crafted by *Hi-D Imaging* using 3D printing technology[51]. The experimental setup replicates the hemodynamics observed in P1 and is initiated from the same *in vivo* segmentation [52].

We used the *in vitro* AV as a template valve for all the patients (by appropriately adapting it to the patient-specific aorta geometry). We have adopted a consistent AV template across multiple patients driven by the substantial time investment required for individualized valve mesh generation. Importantly, our decision is grounded in the consideration that the reference 4D flow MRI data available for our study are consistently acquired in the region downstream of the valve. Consequently, our ability to thoroughly validate the numerical solution in the immediate proximity of the valve is inherently limited.

To produce a generic valve geometry suitable for the whole patient cohort the following pro-

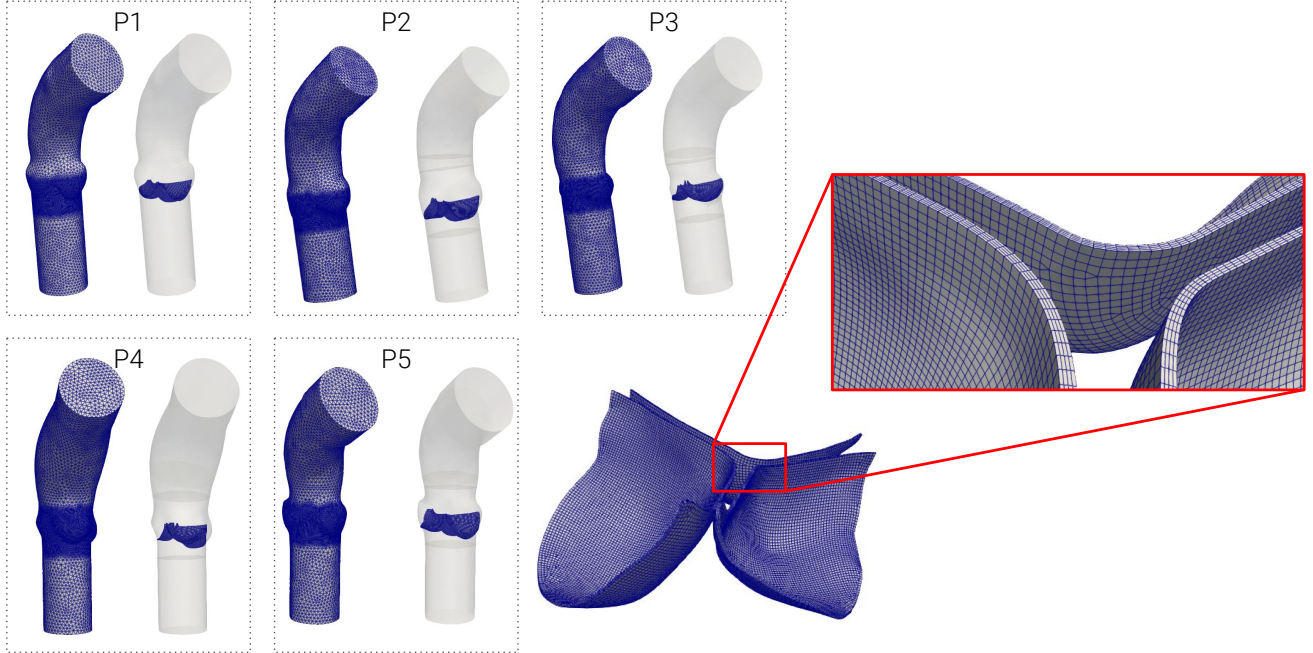


Figure 2: Computational meshes. Left: the five meshes of the aorta and AV; right: the AV solid mesh with a zoom on its thickness.

cedure – illustrated in Figure 1 – is used. We start by extracting the inferior part of the aortic leaflets (i.e. the parts towards the left ventricle) from the 3D model of the *in vitro* setup, obtaining three surfaces. Then, we extend their fixed edges until they perfectly adhere to the computational fluid domain boundaries of P1 (obtained from *in vivo* data). Once the three surfaces are adapted to the aortic wall of the fluid domain, we extrude the leaflets in the normal direction to create a volumetric mesh with a constant thickness equal to 0.3 mm [53]. Since this valve corresponds to patient P1, we conveniently adapt it to be used also with the remaining patients: we position the valve in the region of the Sinus of Valsalva (SoV), we do a rotational alignment to the coronaries, and we scale the geometry according to the diameter of the patient-specific aorta considered.

As for the aorta, the preprocessing of the valve is carried out with the software ANSA [50]: we produce a hybrid hexahedral/pentahedral mesh using four elements in the thickness to capture the bending modes of the valve [24]. The AV mesh is shown in Figure 2 and details of the generated meshes for the solid domains are provided in Table 2.

2.4 Computational model setup

Let Ω_f and Ω_s be the fluid and solid domains, representing an ascending aorta and an AV, respectively (see Figure 4) and let T be the final time. The fluid domain is bounded by Γ_f^{in} , Γ_f^{out} , and Γ_f^w , being the inlet section, outlet section, and wall, respectively. The solid domain is bounded by Γ_s^{wet} and Γ_s^w , being the “wet” part of the aortic leaflets and the portion of the AV attached to the endothelium of the aorta, respectively.

patient	fluid					
	P1	P2	P3	P4	P5	
mesh type	tetrahedra					
h_{\min}	[mm]	0.24	0.14	0.15	0.24	0.25
h_{avg}	[mm]	0.61	0.45	0.46	0.56	0.57
h_{\max}	[mm]	2.58	2.11	2.53	2.55	2.49
# of elements		1 381 518	1 409 841	977 630	1 309 822	1 141 088

patient	solid					
	P1	P2	P3	P4	P5	
mesh type	hybrid hexahedral/pentahedral					
h_{\min}	[mm]	0.0480	0.0742	0.0750	0.0735	0.0730
h_{avg}	[mm]	0.0759	0.0752	0.075 02	0.0745	0.0747
h_{\max}	[mm]	0.1127	0.0747	0.0755	0.075 15	0.0760
# of elements		61 032	58 944	50 848	46 892	57 120

Table 2: Details of the generated meshes: h_{\min} , h_{avg} , and h_{\max} are the minimum, average, and maximum mesh element sizes, respectively. Top: mesh for the aorta; bottom: mesh for the valve leaflets.

The fluid model We consider the blood as an incompressible, viscous, and Newtonian, fluid with constant density $\rho_f = 1100 \text{ kg m}^{-3}$ and constant dynamic viscosity $\mu_f = 3.6 \times 10^{-3} \text{ Pa s}$. Let \mathbf{u}_f and p_f be the fluid velocity and pressure, $\sigma_f(\mathbf{u}_f, p_f) = -p_f \mathbf{I} + \mu_f (\nabla \mathbf{u}_f + \nabla^T \mathbf{u}_f)$ the total stress tensor, the incompressible Navier-Stokes equations endowed with boundary and initial conditions read:

$$\rho_f \left(\frac{\partial \mathbf{u}_f}{\partial t} + (\mathbf{u}_f \cdot \nabla) \mathbf{u}_f \right) - \nabla \cdot \sigma_f(\mathbf{u}_f, p_f) = \mathbf{f} \quad \text{in } \Omega_f \times (0, T), \quad (1)$$

$$\nabla \cdot \mathbf{u}_f = 0 \quad \text{in } \Omega_f \times (0, T), \quad (2)$$

$$\mathbf{u}_f = \mathbf{u}_f^{\text{in}} \quad \text{on } \Gamma_f^{\text{in}} \times (0, T), \quad (3)$$

$$\mathbf{u}_f = \mathbf{0} \quad \text{on } \Gamma_f^{\text{w}} \times (0, T), \quad (4)$$

$$\sigma_f(\mathbf{u}_f, p_f) \mathbf{n}_f = \mathbf{0} \quad \text{on } \Gamma_f^{\text{out}} \times (0, T), \quad (5)$$

$$\mathbf{u}_f = \mathbf{0} \quad \text{in } \Omega_f \times \{0\}. \quad (6)$$

Equation (1) is the momentum balance, with \mathbf{f} a forcing term used to enforce dynamic balance according to the IB method (see below). Equation (2) is the continuity equation. At the inlet section, we set the Dirichlet boundary condition (Equation (3)) by prescribing the inlet flowrate in time and a parabolic profile in space:

$$\mathbf{u}_f^{\text{in}}(\mathbf{x}, t) = -2 \frac{Q_{\text{in}}(t)}{|\Gamma_f^{\text{in}}|} \left(1 - \frac{r^2(\mathbf{x})}{R_{\text{in}}^2} \right) \mathbf{n}_f(\mathbf{x}).$$

where $|\Gamma_f^{\text{in}}|$ is the measure of Γ_f^{in} , $r = |\mathbf{x}|$ is the polar radius coordinate, \mathbf{x} the space coordinate, R_{in} the radius of the inlet section, and \mathbf{n}_f its outward pointing normal. We denote by Q_{in} the inlet flowrate computed with 4D flow MRI, as we explain in Section 2.5. Notice that a parabolic

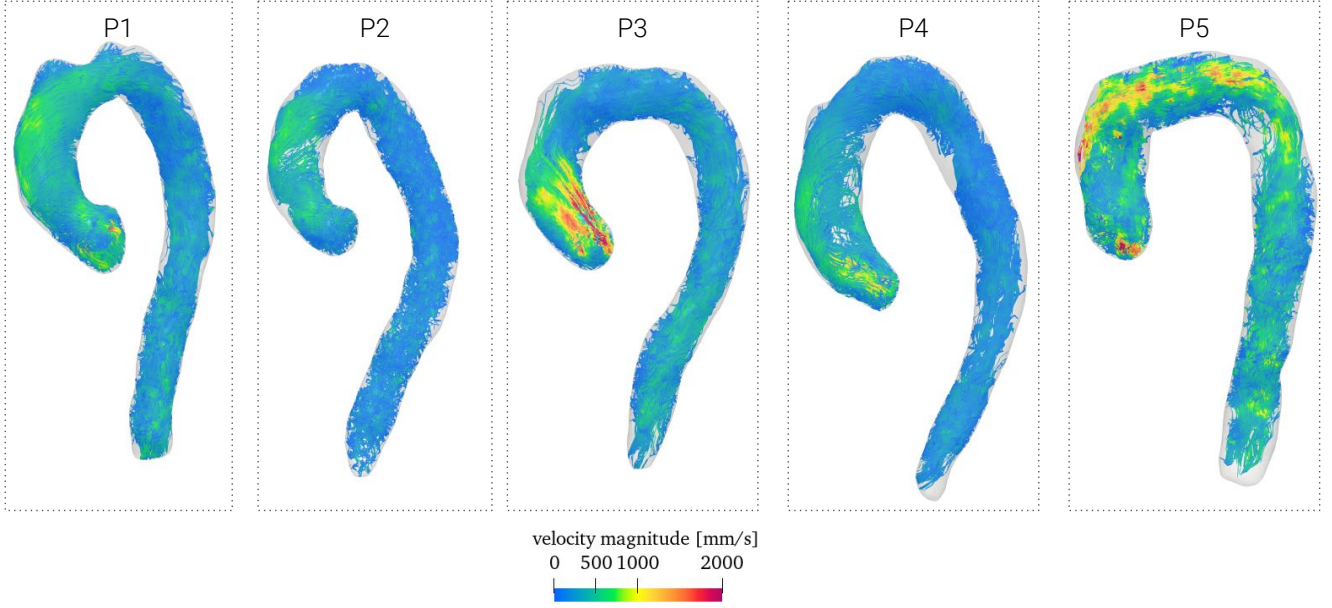


Figure 3: Streamlines obtained with 4D flow MRI at systolic peak for the five patients considered in the study.

profile would in principle correspond to a fully laminar flow. However, we create a flow extension in the inlet long enough so that the flow has space to develop, and our choice of the inlet spatial profile becomes negligible from the region immediately upstream of the AV. On the wall, we set no-slip condition (Equation (4)) and we prescribe homogeneous Neumann boundary condition on the outlet section (Equation (5)). We start the fluid problem with a null initial condition (Equation (6)).

To account for possible transition-to-turbulence effects in the presence of AS [54], we consider a Large Eddy Simulation (LES) model using the eddy viscosity subgrid-scale model proposed by Vreman et al. [55] and used in the vascular context in [56, 57, 22]. Particularly in the context of AS, using a turbulence model might be imperative to capture the small scales when the orifice is small and high-speed jets with large Reynolds numbers are computed [58, 22].

The solid model We model the AV dynamics with the elastodynamic equations in a total Lagrangian formulation. Let Ω_s^0 be the solid domain in its reference (initial) configuration and let \mathbf{X} be the position vector w.r.t. Ω_s^0 . We define $\chi(\mathbf{X}, t)$ as the mapping from the reference to the current configuration so that the displacement of the solid is $\mathbf{d}_s(\mathbf{X}, t) = \chi(\mathbf{X}, t) - \mathbf{X}$. Let ρ_s and ρ_s^0 be the solid density in the current and in the reference configuration, $F = \frac{\partial \chi}{\partial \mathbf{X}}$ the deformation tensor, and its determinant $J = \det(F)$. The elastodynamic equation endowed with boundary and initial conditions reads:

$$\rho_s^0 \frac{\partial^2 \mathbf{d}_s}{\partial t^2} - \nabla_0 \cdot P(\mathbf{d}_s) = \mathbf{0} \quad \text{in } \Omega_s^0 \times (0, T), \quad (7)$$

$$\rho_s^0 J^0 = \rho_s J \quad \text{in } \Omega_s^0 \times (0, T), \quad (8)$$

$$\mathbf{d}_s = \mathbf{0} \quad \text{on } \Gamma_s^w \times (0, T), \quad (9)$$

$$\frac{\partial \mathbf{d}_s}{\partial t} = \mathbf{0} \quad \text{in } \Omega_s^0 \times \{0\}, \quad (10)$$

$$P(\mathbf{d}_s) = \mathbf{0} \quad \text{in } \Omega_s^0 \times \{0\}, \quad (11)$$

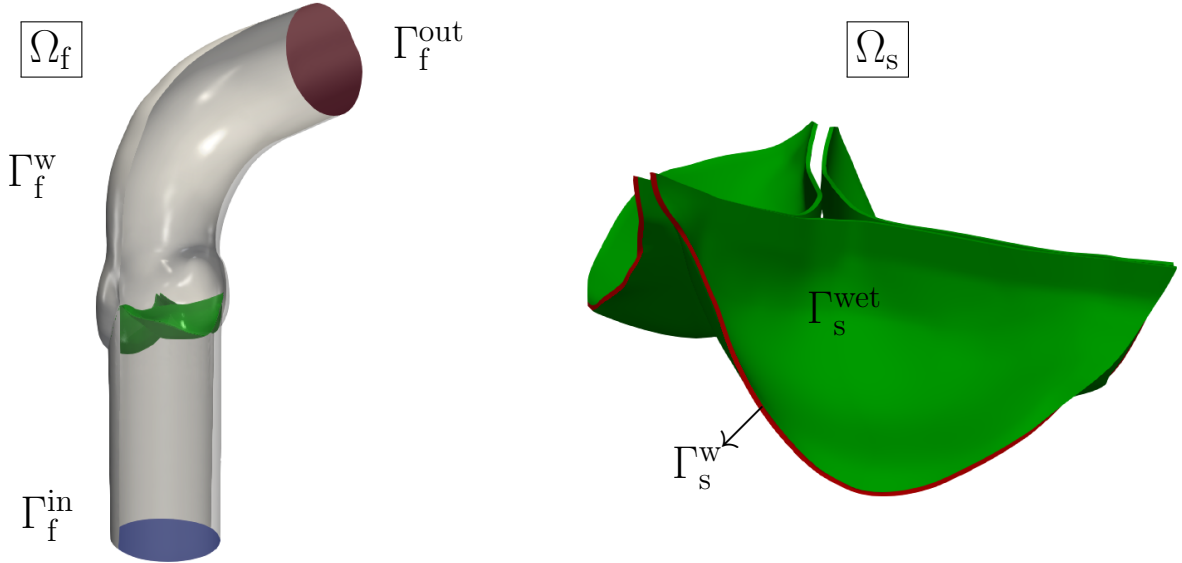


Figure 4: Computational domain. Left: the fluid domain Ω_f bounded by inlet section Γ_f^{in} , outlet section Γ_f^{out} and wall Γ_f^w . Right: the solid domain Ω_s bounded by Γ_s^w and Γ_s^{wet} .

where Equation (7) is the momentum balance, with P the nominal stress tensor. Equation (8) is the mass conservation, we set a homogeneous Dirichlet condition on Γ_s^w (Equation (9)), and we initialize our problem with null initial conditions (Equation (10), Equation (11)). The material of the AV is primarily characterized by an isotropic extracellular matrix and anisotropic alignment of collagen fibers. However, for simplicity, we adopt an isotropic Neo-Hookean material model with Lamé coefficients λ_s and μ_s [59, 24]. Our choice of this simplified constitutive law is tailored to the specific objectives of our work, deemed adequate for validating blood flow downstream of the valve. Furthermore, our selection is in line with other studies in the literature [32, 60, 24].

The IB model for FSI We consider a fully-coupled FSI model based on the IB method [48, 27]. Dynamic balance between the fluid and solid model is enforced by defining the forcing term in the Navier Stokes' momentum balance (1) as:

$$\mathbf{f}(\mathbf{x}, t) = \int_{\Omega_s^0} \nabla_0 \cdot P(\mathbf{X}, t) \delta(\mathbf{x} - \chi(\mathbf{X}, t)) d\mathbf{X}, \quad \text{with } \mathbf{x} \in \Omega_f, t \in (0, T), \quad (12)$$

and δ is a 3D Dirac delta distribution. Conversely, continuity of velocity between the fluid and the structure is enforced through the following kinematic condition:

$$\frac{\partial \mathbf{d}_s}{\partial t} = \int_{\Omega_f} \mathbf{u}_f(\mathbf{x}, t) \delta(\chi(\mathbf{X}, t) - \mathbf{x}) d\mathbf{x} \quad \text{with } \mathbf{X} \in \Omega_s^0, t \in (0, T). \quad (13)$$

Numerical methods We discretize the fluid dynamics problem in space with the Finite Element (FE) method with linear FE spaces for both velocity and pressure. Time integration is carried out using an explicit third order Runge-Kutta method (with CFL = 0.8) and we impose the divergence-free constraint (2) with a fractional-step scheme. For additional details on the numerical schemes we used for the fluid problem, we refer the reader to [61]. The elastodynamic equation is solved with FE method with quadratic FE space, a generalized Newmark formulation as time advancing

patient		P1	P2	P3	P4	P5
T (physical time)	[s]	10.6	10.2	7.1	7.1	6.8
CPU time	[hours]	129.6	124.8	86.4	86.4	81.6

Table 3: Computational times of the FSI simulations. For each patient, we simulate ten heartbeats.

scheme. To solve the fully-coupled FSI problem, we use an explicit staggered coupling scheme: given the solution at a discrete time, we advance the time step by first solving the fluid dynamics problem, we interpolate \mathbf{u}_f to Ω_s^0 (kinematic coupling condition (13)), we compute the displacement by integrating the interpolated velocity with a first-order Euler scheme, and we displace accordingly the solid domain; we compute the internal forces of the structure and we compute the forcing term (12), enforcing the dynamic balance. For additional details on the IB-FSI scheme, we refer to [24].

Computational setup The computational model is implemented in the multiphysics and multiscale FE library ALYA [62, 63] developed at the Barcelona Supercomputing Center and designed to run efficiently on supercomputers in a High Performance Computing (HPC) framework to simulate tightly coupled problems. We use a constant time step size equal to 5×10^{-6} s for both the fluid and solid problem. To execute efficiently the code, two ALYA parallel instances are simultaneously executed, one for the fluid and one for the solid problem. At every time step, the two instances communicate with each other through a point-to-point scheme programmed using MPI-communicators. We use 568 and 256 cores for the fluid and solid problem, respectively. For additional details on the parallelization strategy of the AV FSI model we deployed in ALYA, we refer the reader to [24]. We carry simulations on the ARCHER2 UK National Supercomputing Service² and the Nord 3 machine³ at the Barcelona Supercomputing Center. We report computational times of the five simulations in Table 3: the average cost of simulating a heart cycle is around 10 hours.

2.5 Feeding the FSI model with the *in vivo* flowrate

Considering that the paper aims to validate the blood flow in the region downstream the AV, we define a Region of Interest (ROI) as we display in Figure 5. Several QoIs are computed and averaged in this control volume.

To set boundary conditions on the inlet of the aorta, we compute the flowrate from the 4D flow MRI data. As displayed in Figure 5, we compute the flowrate in five different planes Γ_j belonging to the ROI as

$$Q_{\Gamma_j}^{4D\text{flow}}(t) = \int_{\Gamma_j} \langle \mathbf{u}^{4D\text{flow}}(\mathbf{x}, t) \rangle \cdot \mathbf{n}(\mathbf{x}, t) d\mathbf{x}, \quad \text{with } j = 1, \dots, 5, \quad (14)$$

where \mathbf{n} the normal to the plane Γ_j considered. As illustrated in Figure 5, notable variations exist in the computed flowrates among different sections, potentially attributed to the combined influences of aortic wall compliance and noise. To address these factors and include them in the

²<https://www.archer2.ac.uk>

³<https://www.bsc.es/marenostrum>

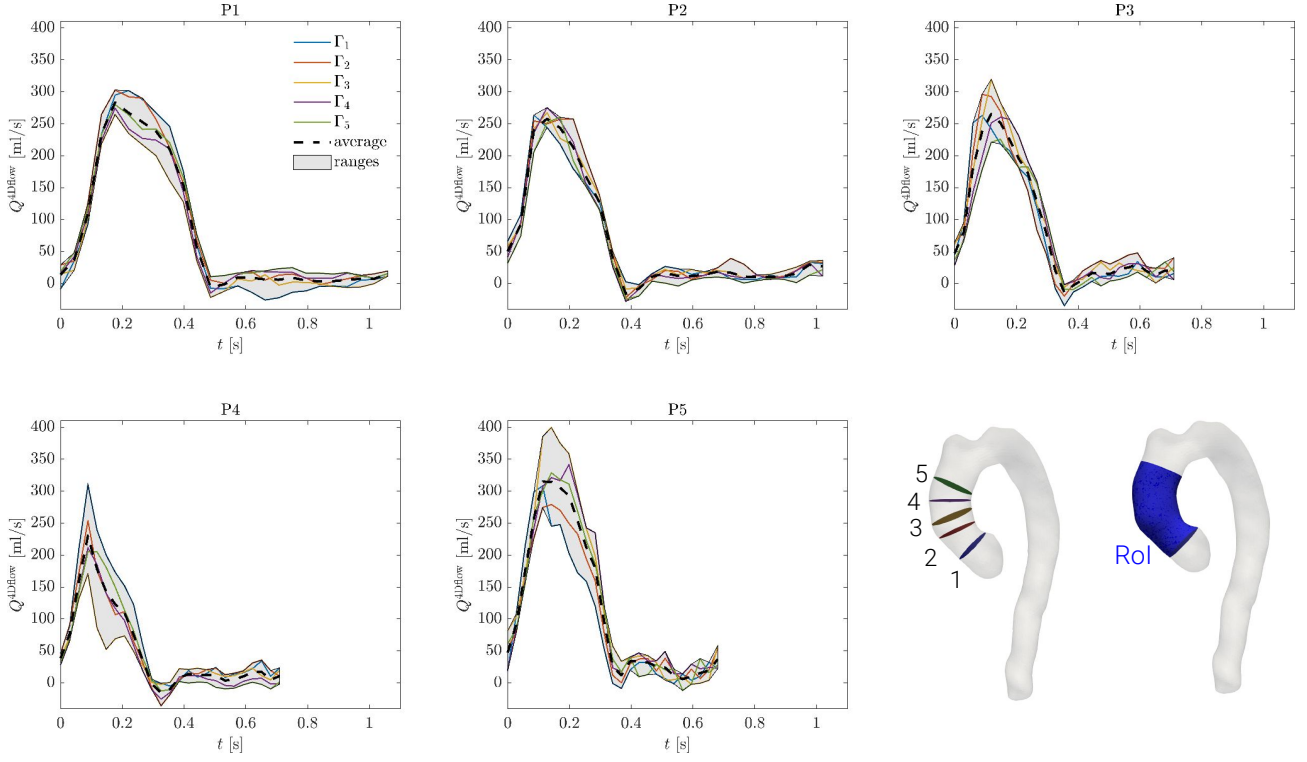


Figure 5: Flowrate in different planes computed from the 4D flow MRI data. In each plot, we report the flowrate computed in a different plane of the ROI, the average, and the ranges to highlight the spatial variability of these data.

computational model, we compute the average of these flowrates and use it as our inlet flowrate:

$$Q_{\text{in}}(t) = Q_{\text{avg}}^{\text{4Dflow}}(t) = \frac{1}{5} \sum_{j=1}^5 Q_{\Gamma_j}^{\text{4Dflow}}(t). \quad (15)$$

In Figure 5, we show shaded regions to accommodate the flowrate’s variability. Moreover, to ensure that the AV remains closed during diastole, we set $Q_{\text{in}} = 0$ during this phase. Furthermore, since the 4D flow MRI flowrate is characterized by a poorer time resolution compared to the one required by the FSI problem, we use B-splines to approximate and smooth this temporal function in time.

2.6 Calibration of the Young modulus of the AV

To carry out FSI simulations of the AV, it is crucial to accurately select the parameters of the structural model of the valve, parameters that might be patient-specific and also related to the stenosis level. We set the density value to $\rho_s = 1000 \text{ kg m}^{-3}$. Regarding the Lamé constants – which are related to the Young modulus E_s and the Poisson’s ratio ν_s – we fix $\nu_s = 0.3$, and we calibrate E_s to match the Mean Kinetic Energy (MKE) per unit mass of the 4D flow MRI data downstream of the AV within the ROI for patient P1.

Spreading the uncertainty of the flowrate onto the MKE To spread the uncertainty of the inlet flowrate into the kinetic energy (see Figure 5), in the following, we establish ranges of

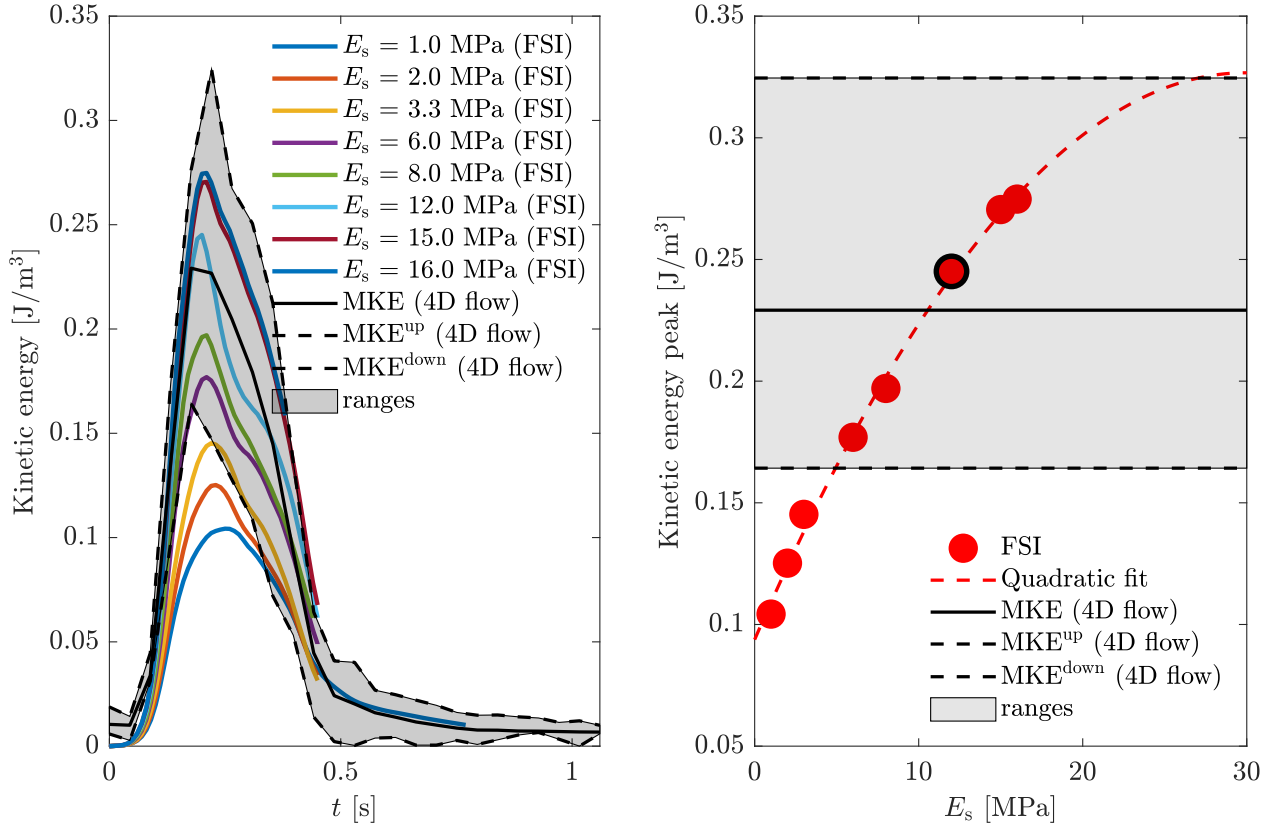


Figure 6: Calibration of the Young modulus E_s for P1 to get an accurate representation of the kinetic energy in the ROI. Left: temporal evolution of the MKE obtained by eight different Young modulus and the *in vivo* 4D flow MRI data. Right: peak of kinetic energies for the eight setups of the FSI model against peak from 4D flow MRI data (with corresponding range), with quadratic fit of the FSI results.

uncertainty for the MKE. Recalling that ρ_f is constant, we define the MKE per unit mass as:

$$\text{MKE}(t) = \frac{1}{2|\Omega_f^{\text{ROI}}|} \int_{\Omega_f^{\text{ROI}}} |\langle \mathbf{u}^{4\text{Dflow}}(\mathbf{x}, t) \rangle|^2 d\mathbf{x}, \quad (16)$$

where $|\Omega_f^{\text{ROI}}|$ is the volume of the ROI. We then define the upper and lower MKE as

$$\text{MKE}^{\text{up}}(t) = \text{MKE}(t) + \delta^{\text{up}}(t)\text{MKE}(t), \quad (17)$$

$$\text{MKE}^{\text{down}}(t) = \text{MKE}(t) - \delta^{\text{down}}(t)\text{MKE}(t), \quad (18)$$

where $\delta^{\text{up}} \in [0, 1]$ and $\delta^{\text{down}} \in [0, 1]$ are the upper and lower relative variations with respect to the averaged MKE. These ranges encompass variations in aortic blood flow rates arising from 4D flow MRI acquisitions noise and aortic compliance, which is not considered in the computational model. To compute kinetic energy uncertainty, we derive minimum, maximum, and average velocities from flow measurements, and then integrate the square of those data into the kinetic energy computation. Further elaboration on this process follows. Considering Equation (14), we define the minimum and maximum measured flowrates for all the N time frames of the 4D flow MRI acquisition as:

$$Q_{\min}^{4\text{Dflow}}(t_i) = \min_j Q_{\Gamma_j}^{4\text{Dflow}}(t_i), \quad Q_{\max}^{4\text{Dflow}}(t_i) = \max_j Q_{\Gamma_j}^{4\text{Dflow}}(t_i), \quad \text{for all } i = 1, \dots, N. \quad (19)$$

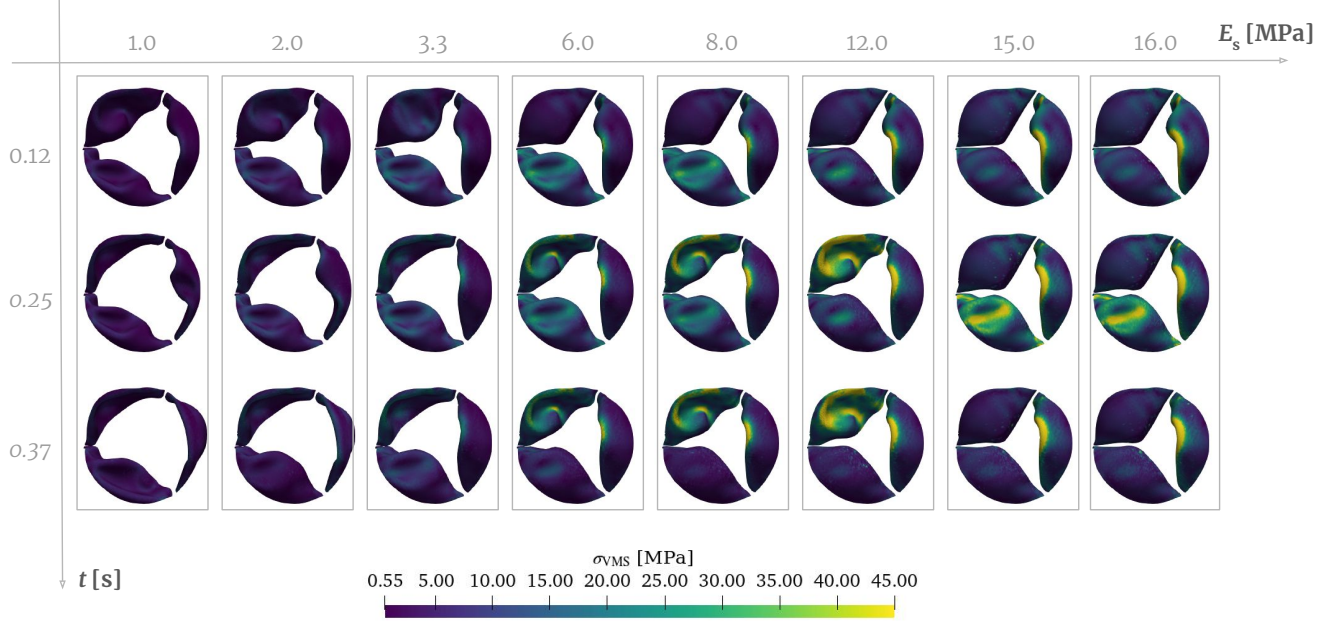


Figure 7: AV in three different instants of the heart cycle ($t = 0.12$ s, $t = 0.25$ s, and $t = 0.37$ s) for different values of the Young modulus E_s . The AV is colored according to the von Mises stress.

Let $A_{Q_{\min}}(t_i)$ and $A_{Q_{\max}}(t_i)$ be the area of the section corresponding to the minimum and maximum flowrate computed in Equation (19), and let $A_{\text{avg}}(t_i)$ be the average area of the sections at time t_i , with $i = 1, \dots, N$. We define the average, minimum, and maximum velocity – constant in space – corresponding to the flowrates in Equations (15) and (19) as:

$$\tilde{\mathbf{u}}_{\text{avg}}(t_i) = \frac{Q_{\text{avg}}^{\text{4Dflow}}(t_i)}{A_{\text{avg}}(t_i)}, \quad \tilde{\mathbf{u}}_{\min}(t_i) = \frac{Q_{\min}^{\text{4Dflow}}(t_i)}{A_{Q_{\min}}(t_i)}, \quad \tilde{\mathbf{u}}_{\max}(t_i) = \frac{Q_{\max}^{\text{4Dflow}}(t_i)}{A_{Q_{\max}}(t_i)}, \quad \text{for all } i = 1, \dots, N.$$

To compute the corresponding MKEs in the ROI, since $\tilde{\mathbf{u}}_{\text{avg}}$, $\tilde{\mathbf{u}}_{\min}$, and $\tilde{\mathbf{u}}_{\max}$ are constant in space, the associated kinetic energies are simply defined as:

$$\widetilde{\text{MKE}}^{\text{avg}}(t_i) = \frac{1}{2|\Omega_f^{\text{ROI}}|} \tilde{\mathbf{u}}_{\text{avg}}^2(t_i), \quad \widetilde{\text{MKE}}^{\min}(t_i) = \frac{1}{2|\Omega_f^{\text{ROI}}|} \tilde{\mathbf{u}}_{\min}^2(t_i), \quad \widetilde{\text{MKE}}^{\max}(t_i) = \frac{1}{2|\Omega_f^{\text{ROI}}|} \tilde{\mathbf{u}}_{\max}^2(t_i).$$

We then define the relative upper and lower variations as:

$$\delta^{\text{up}}(t_i) = \frac{|\widetilde{\text{MKE}}^{\max}(t_i) - \widetilde{\text{MKE}}^{\text{avg}}(t_i)|}{\max(\widetilde{\text{MKE}}^{\max}(t_i), \widetilde{\text{MKE}}^{\text{avg}}(t_i))}, \quad \text{for all } i = 1, \dots, N,$$

$$\delta^{\text{down}}(t_i) = \frac{|\widetilde{\text{MKE}}^{\min}(t_i) - \widetilde{\text{MKE}}^{\text{avg}}(t_i)|}{\max(\widetilde{\text{MKE}}^{\min}(t_i), \widetilde{\text{MKE}}^{\text{avg}}(t_i))}, \quad \text{for all } i = 1, \dots, N.$$

Notice that we define the relative changes as above to avoid division by very small numbers [64].

Calibration of the Young modulus We calibrate the Young modulus for patient P1 using the following values:

$$E_s = [1.0, 2.0, 3.3, 6.0, 8.0, 12.0, 15.0, 16.0] \text{ MPa.}$$

For this calibration process, simulations were conducted for less than one heartbeat since the tuning of the Young modulus is based solely on the peak kinetic energy. Thus, to be precise, we compare here the MKE (i.e. with phase-averaged velocity) from 4D flow MRI against the kinetic energy (i.e. from the velocity in the first beat) from FSI.

Figure 6 illustrates the results of our calibration process: as the Young modulus increases, the computed values approach our reference values from 4D flow MRI data. It is important to note that, for the 4D flow MRI data, we present both the actual MKE computed in the ROI and the corresponding variations due to the uncertainty of the flowrate, as explained earlier. In Figure 7, we display the AV in three different instants of the heartbeat for the values considered of the Young modulus. As expected, as E_s increases, we observe a smaller orifice area, resulting in a faster blood jet (since the inlet flowrate remains constant). Furthermore, as the Young modulus increases, we compute larger values of the von Mises stress σ_{VMS} , an indicator that can be used to assess the calcification level of the AV [24].

The calibration study allows us to establish that $E_s = 12$ MPa accurately replicates the 4D flow MRI data for P1, providing computational kinetic energy values within the range of variation of the *in vivo* 4D flow MRI and closer to the computed MKE. Consequently, we select this value of the Young modulus for the entire study. Consistency is maintained by applying the same Young modulus value to the remaining patients, given their similar severity levels of AS. Moreover, this decision expedites the calibration process across the entire study.

3 Results

We present the results of our study. We validate our results against *in vivo* data in Section 3.1, whereas in Section 3.2, we present additional QoIs computed with the FSI simulations useful for AS assessment.

3.1 Validation

We validate the *in silico* results against 4D flow MRI velocity data. In particular, since the *in vivo* data consists on phase-averaged velocity fields, we run our FSI simulations for ten heartbeats, we discard the first two cycles to remove the influence of null initial conditions, and we phase-average the velocity in the remaining eight cycles as [65]:

$$\langle \mathbf{u}_f(\mathbf{x}, t) \rangle = \frac{1}{8} \sum_{n=3}^{10} \mathbf{u}_f(\mathbf{x}, t + (n - 1)T_{\text{HB}}).$$

Figure 8 illustrates the validation of $\langle \mathbf{u}_f \rangle$ for all five patients at the systolic peak. Specifically, we compare the velocity along a clip in the longitudinal direction of the aorta and three slices within the ROI. Our findings indicate that, except for P2 and P3, the FSI model accurately reproduces the flow patterns observed in the *in vivo* data. This includes a faithful capture of the strong jet crossing the AV, along with its impingement on the wall. Additionally, when considering the slices within the ROI, we observe a similar spatial velocity distribution between the computational results and the *in vivo* data. We believe that the discrepancy in the velocity patterns observed for P2 and P3 might be due to the use of the same valve geometry among different patients.

To quantitatively assess the disparity between the computational results and the 4D flow MRI data, we calculate the MKE within the region of interest using Equation (16) with $\langle \mathbf{u}_f \rangle$. Figure 9

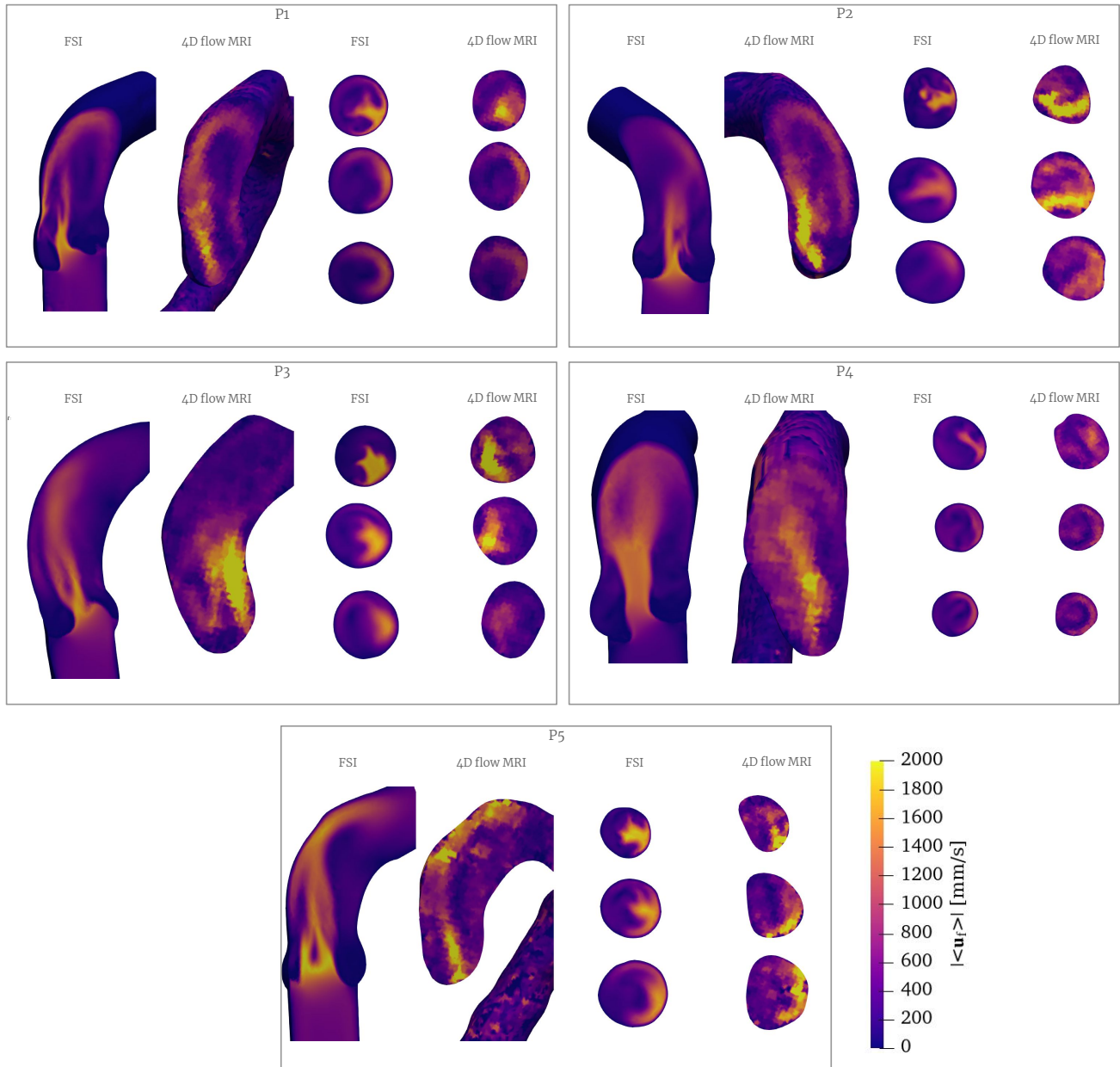


Figure 8: Validation of phase-averaged velocity magnitude against 4D flow MRI data at the systolic peak for the five patients. For each patient, results are compared on a clip in the longitudinal direction of the ascending aorta, and on three slices in the ROI.

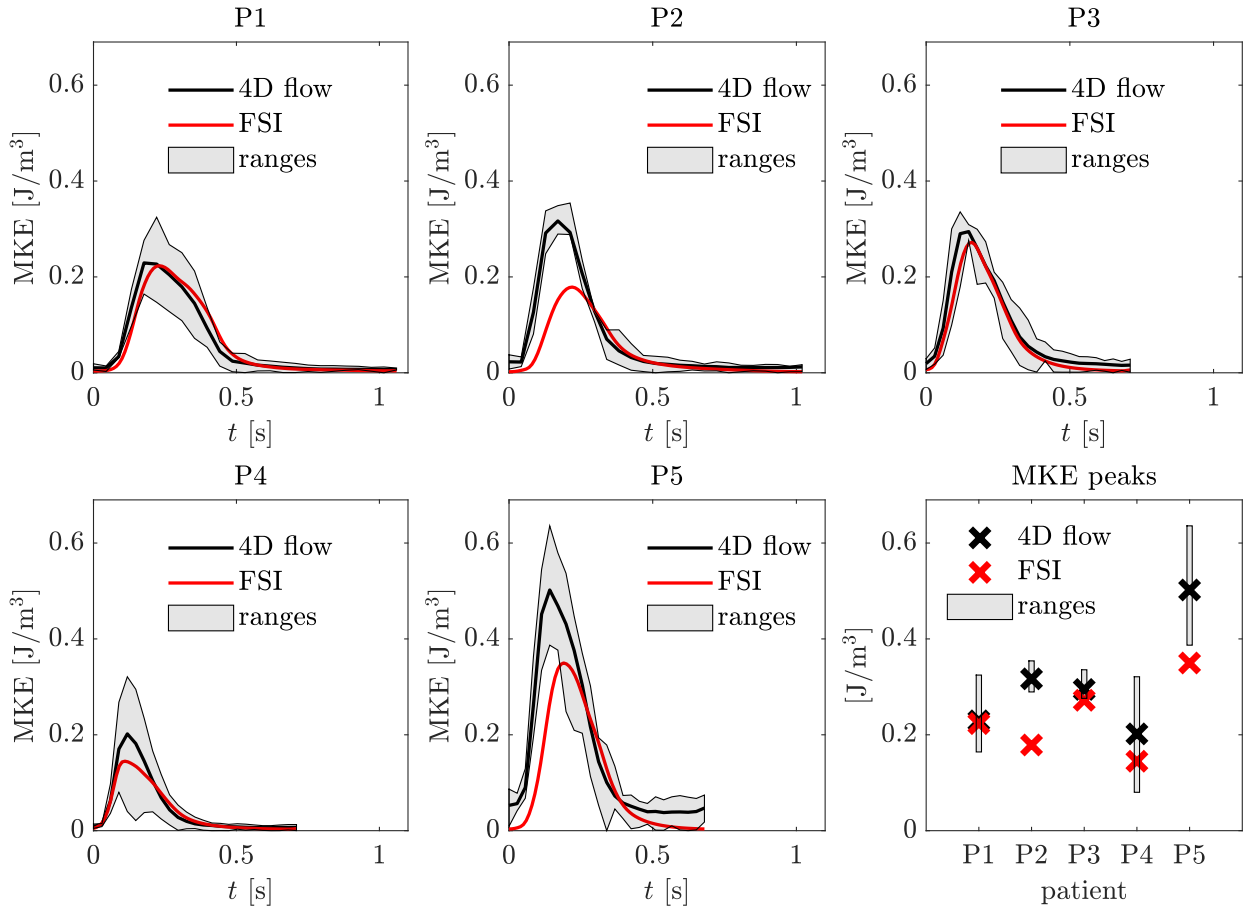


Figure 9: Validation of MKE against 4D flow MRI data for the five patients.

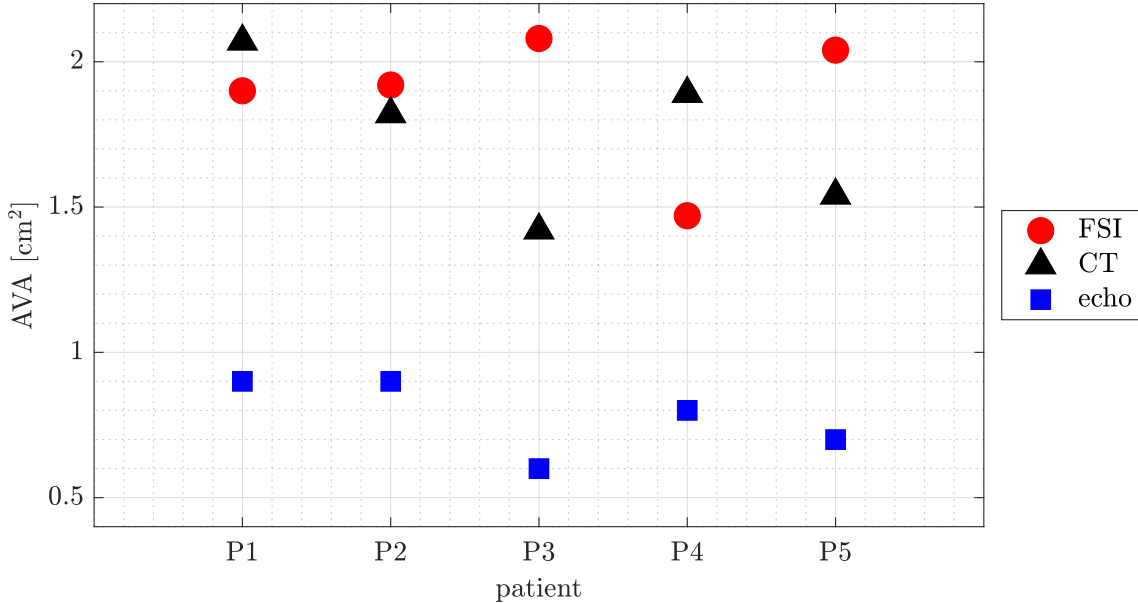


Figure 10: AVA measurements: comparison between FSI, CT measurement and echo measurement.

presents a comparison of the MKE, incorporating the ranges of variations detailed in Section 2.5. As expected, larger variations of the flowrate correspond to larger variations of the MKE. Notably, with the exception of P2, the computational results exhibit a temporal evolution closely resembling that of the *in vivo* data, with most patients' computational MKE falling within the range of variations observed in the 4D flow MRI data. The discrepancy for patient P2 is consistent with the larger velocity observed in Figure 8. Interestingly, despite discrepancies in the flow patterns of P3, the model accurately reproduces its kinetic energy. In Figure 9, we also provide a comparison of the MKE peaks for the five patients, showing that the peaks are always within the ranges of uncertainty, except for P2 and P5: for both patients, we underestimate the *in vivo* MKE peak. Notice also that, since the calibration process is carried out for P1 only, and the same value of E_s is then used for the remaining patients, it is reasonable to expect a better accuracy for P1 than the remaining ones.

We compare the orifice area (or AVA) using computational and *in vivo* measurements. From the FSI simulations, we compute the Geometric Orifice Area (GOA) as the area enclosed by the projection of the leaflet commissure curves on the aortic cross section [24]. Furthermore, clinicians carried out echocardiography measurements to compute the AVA via continuity equation method [66]. In Figure 10, we compare the AVA using FSI and echo measurements: *in silico* simulations give AVA results in the order of two/three times larger than *in vivo* measurements. Differently, by measuring directly the AVA from the static CT images, we obtain values that are much more in line with the computational results, resulting in a mean relative error of 23%. This explains that the main source of error might come from the measurement method (continuity-based vs. geometrical).

To assess the reliability of the computational model in terms of shear stress, we compute several quantities inside the fluid domain and on its boundary. Let $\tau_f(\langle \mathbf{u}_f \rangle) = \mu_f(\nabla \langle \mathbf{u}_f \rangle + \nabla^T \langle \mathbf{u}_f \rangle)$ be the

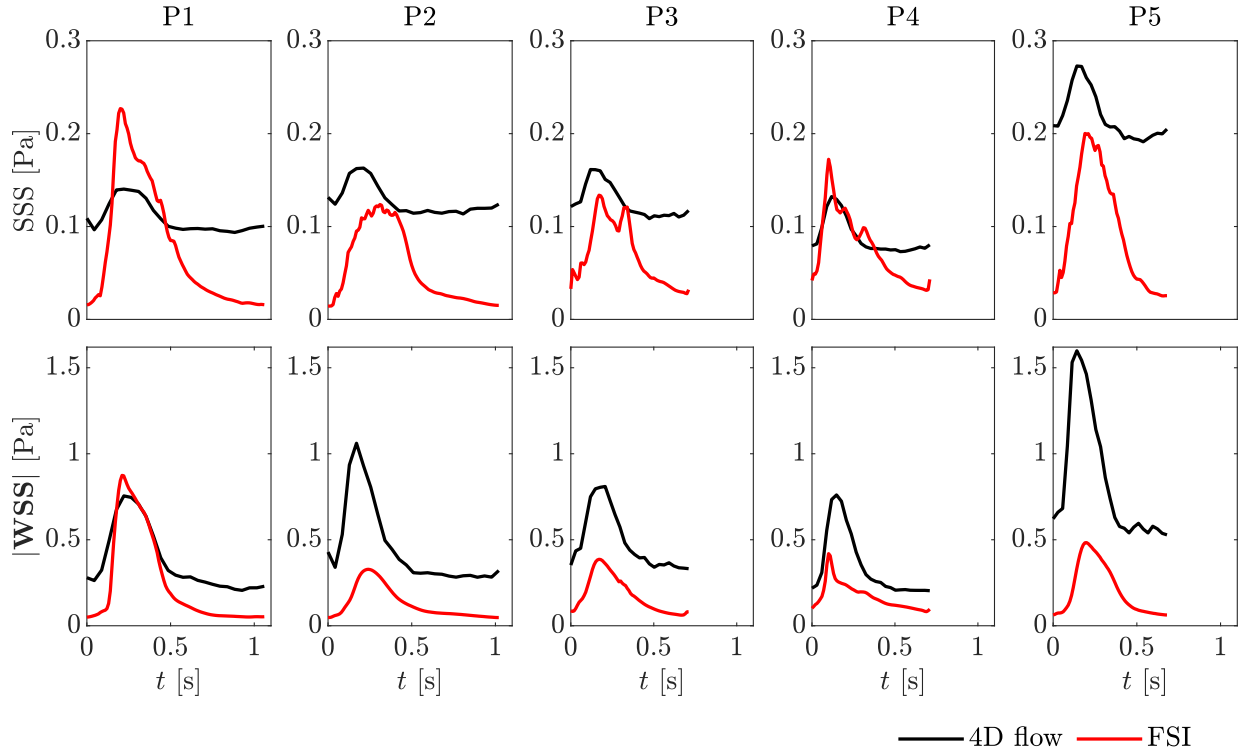


Figure 11: Validation of space-averaged SSS (top) and space-averaged WSS magnitude (bottom) against 4D flow MRI data for the five patients.

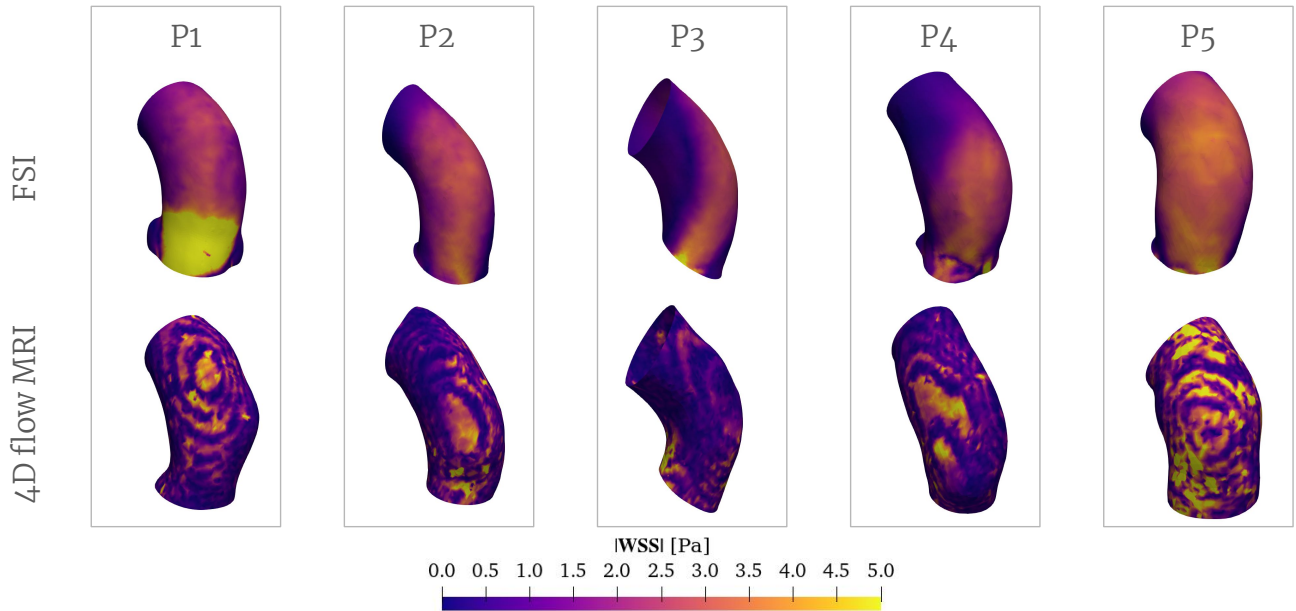


Figure 12: Validation of WSS in the ROI. Top: FSI; bottom: 4D flow MRI.

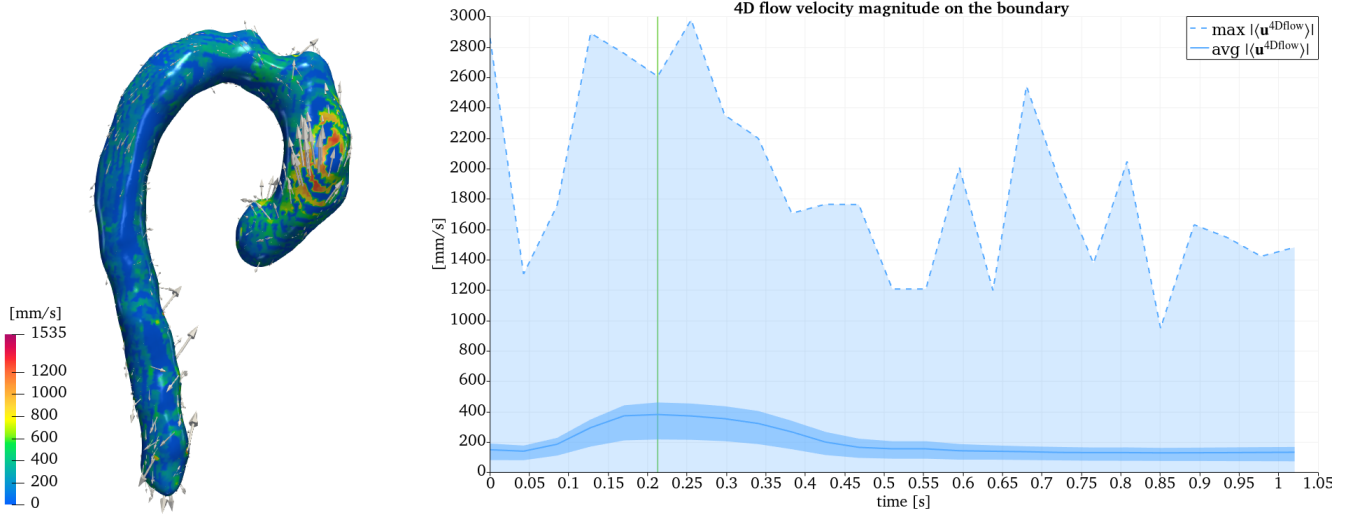


Figure 13: 4D flow MRI velocity on the boundary for P1. On the left, a visualization of the velocity on the wall of the aorta at the systolic peak. To the right, the time series of the maximum, average and quartile velocity on the aorta boundary.

viscous stress tensor, we compute the Scalar Shear Stress (SSS) as [67]:

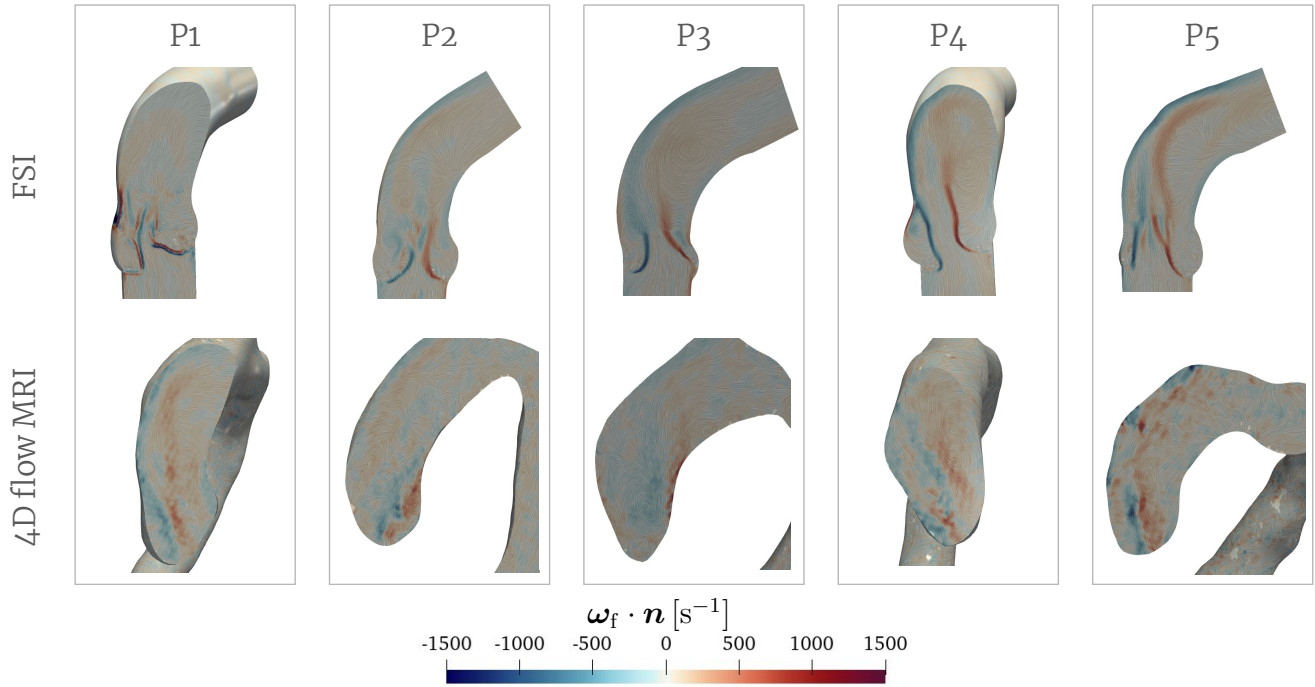
$$\text{SSS}(\mathbf{x}, t) = \sqrt{\frac{1}{6} \sum_{i=1}^3 \sum_{\substack{j=1 \\ j \neq i}}^3 \left((\tau_{f_{ii}} - \tau_{f_{jj}})^2 + \tau_{f_{ij}}^2 \right)}, \quad \text{in } \Omega_f \times (0, T_{\text{HB}})$$

and the Wall Shear Stress (WSS) on the boundary of the fluid domain as:

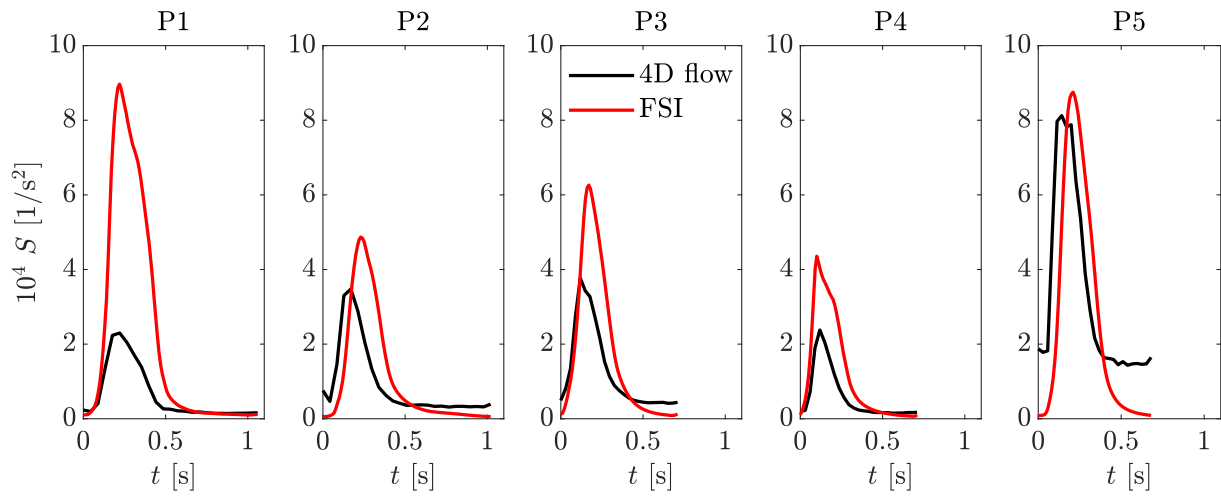
$$\mathbf{WSS}(\mathbf{x}, t) = \tau_f(\langle \mathbf{u}_f \rangle) \mathbf{n}_f - (\tau_f(\langle \mathbf{u}_f \rangle) \mathbf{n}_f \cdot \mathbf{n}_f) \mathbf{n}_f, \quad \text{on } \partial\Omega_f \times (0, T_{\text{HB}}).$$

We compare the SSS and the WSS for the five patients against 4D flow MRI data: in Figure 11 we compare the space-averaged SSS and the space-averaged WSS magnitude. In all the cases, the FSI simulation produces profiles similar to the 4D flow MRI, where large values of both indicators are measured during the ejection phase. However, some discrepancies in terms of values are observed. For SSS, there are cases where the FSI underestimates the 4D flow MRI data, while in others, the computational results yield larger values. Concerning WSS, a general trend emerges where, except for P1, the FSI produces lower values. This trend aligns with the observations for the MKE in Figure 9, potentially also accentuated by the lower resolution of the 4D flow MRI data compared to the FSI simulations, which, along with the noise characterizing the *in vivo* data, may highly affect the accuracy of velocity gradient computations. As we illustrate in Figure 13, the 4D flow MRI data are often characterized by large and unrealistic velocities and velocity gradients at the wall in localized regions. Thus, this strongly affects the reliability of *in vivo* stress quantities at the wall, especially since velocity derivatives are involved.

In Figure 12, we report the WSS at the systolic peak on the boundary of the ROI. The field computed with the 4D flow MRI data appears not very regular. Nonetheless, generally speaking we can observe that, for both FSI and 4D flow MRI, as the blood accelerates through the AV leaflets and impinges the aortic wall, larger values of the WSS are measured. In P1, we observe larger values of the stress in the lower part of the ROI that are not found in the *in vivo* data. Furthermore, for P3, we fail to reproduce the region with larger WSS and this is consistent with the discrepancy of the flow pattern observed in Figure 8.



(a)



(b)

Figure 14: Validation of vorticity and enstrophy a) validation of the projection of the vorticity in the normal direction of a plane of the aorta (top, FSI; bottom, 4D flow MRI). (b) Validation of enstrophy S : in red, FSI; in black, 4D flow MRI.

Next, we assess the accuracy of the model in terms of its ability to capture the vorticity and the enstrophy. Let $\boldsymbol{\omega}_f = \nabla \times \langle \mathbf{u}_f \rangle$ be the vorticity computed with the phase-averaged velocity; we compute the enstrophy per unit mass in the ROI as:

$$S(t) = \frac{1}{|\Omega_f^{\text{ROI}}|} \int_{\Omega_f^{\text{ROI}}} |\boldsymbol{\omega}_f|^2 d\mathbf{x}.$$

In Figure 14a, we display the projection of the vorticity in the normal direction of a plane of the aorta ($\boldsymbol{\omega}_f \cdot \mathbf{n}$) using the FSI simulations and 4D flow MRI data. In the same plane, we also report surface Line Integral Convolution (LIC) of the phase-average velocity, to better appreciate the formation of vortices. In all cases, we can observe shear layers forming on the leaflets of the AV producing counter-rotating vortices into the Valsalva sinuses, a well-known physiological pattern [68, 69]. Similar patterns between FSI and 4D flow MRI are observed for all the patients except P3, consistently with the previous results on velocity and WSS. Furthermore, due to the lower resolution and the noise of the *in vivo* data, the numerical simulations provide a much more detailed visualization of the vorticity field, allowing for a better inspection of vortices and shear layers.

In Figure 14b, we present the space-averaged enstrophy. Across all cases, our computational model accurately tracks the temporal evolution observed in the *in vivo* data. However, we note that the enstrophy values derived from the FSI simulations consistently surpass those from the *in vivo* measurements. This discrepancy may stem from the lower reliability of 4D flow MRI in computing velocity derivatives, as we discussed for the WSS validation.

3.2 Additional QoIs from FSI simulations

After validating the results, we demonstrate the utility of FSI in computing additional QoIs essential for assessing AS. While 4D flow MRI enables the quantification of several phase-averaged hemodynamic parameters related to blood flow, including mean velocity, MKE, and shear stress resulting from mean flow, the following section focuses on extracting further QoIs from FSI simulations specifically beneficial for AS assessment, beyond the scope of validation.

AS patients are often characterized by increased turbulence that can be estimated by the Turbulent Kinetic Energy (TKE) of the blood flow [41]. By defining the root mean squared velocity as $\mathbf{u}'(\mathbf{x}, t) = \sqrt{\langle \mathbf{u}_f^2(\mathbf{x}, t) \rangle - \langle \mathbf{u}_f(\mathbf{x}, t) \rangle^2}$, we compute the TKE as [70, 65]

$$\text{TKE}(t) = \frac{1}{2|\Omega_f^{\text{ROI}}|} \int_{\Omega_f^{\text{ROI}}} \mathbf{u}'(\mathbf{x}, t)^2 d\mathbf{x}.$$

Furthermore, since patients with AS are characterized by large pressure gradients [71, 72], we compute the TPG by averaging the pressure in a slice upstream and a slice downstream the AV:

$$\text{TPG}(t) = \frac{1}{|\Gamma_{\text{down}}|} \int_{\Gamma_{\text{down}}} p_f(\mathbf{x}, t) d\mathbf{x} - \frac{1}{|\Gamma_{\text{up}}|} \int_{\Gamma_{\text{up}}} p_f(\mathbf{x}, t) d\mathbf{x}.$$

We report the TKE and the TPG for the five patients in Figure 15. By averaging these results among the five patients, we get an average TKE peak of 15.8 J m^{-3} and an average TPG peak of around 13 mmHg.

Finally, in the context of AS and TAVR, assessing the probability of thrombus formation is crucial. Regions with elevated thrombotic risk can be identified by analyzing the residence time

of the blood: longer residence times correlate with heightened thrombotic risk [73]. To compute the residence time, we employ an Eulerian approach by advecting a passive scalar $T_r(\mathbf{x}, t)$ in the fluid [24]:

$$\begin{aligned} \frac{\partial T_r}{\partial t} + \nabla \cdot (\mathbf{u}_f T_r) &= 1 && \text{in } \Omega_f \times (0, T), \\ T_r &= 0 && \text{on } \Gamma_f^{\text{in}} \times (0, T), \\ \nabla T_r \cdot \mathbf{n}_f &= 0 && \text{on } \Gamma_f^{\text{w}} \cup \Gamma_f^{\text{out}} \times (0, T). \end{aligned}$$

Figure 16 illustrates the residence time (T_r) for the five patients during systole and diastole. In both phases of the cardiac cycle, we observe an increase in residence time in the region of SoV, potentially leading to reduced blood washout and increased thrombogenic potential. Consequently, variations in the washout of sinus flow and the presence of stasis regions among different patient models – described by the residence time – may contribute to varying risks of leaflet thrombosis and/or valve’s leaflets degeneration [74]. In Figure 15, we report the residence time averaged in the ROI: after a few cycles, the solution becomes periodic and particles stay in the ROI for about 1.8 s (by averaging the solution among all the patients).

4 Discussion

We presented a study aimed at validating the blood downstream of the AV using FSI computational modeling against 4D flow MRI data.

Upon examining the 4D flow MRI data, we observed significant variations in flow rate between different sections. While it was expected for the aorta to exhibit varying flow rates due to its compliance, the magnitude of these variations seemed excessive, considering the standard compliance of the aorta, which typically results in approximately a 10% enlargement of its diameter [75]. Additionally, upon computing the divergence of the 4D velocity, we observed a significant deviation from the incompressibility constraint. The accuracy of 4D flow MRI acquisition strongly depends on several parameters such as spatial resolution, signal-to-noise ratio, and non-Gaussian intravoxel velocity distributions [76, 77]. In addition, signal loss near the AV compromised the accuracy of these data in this region, making the validation process more challenging [76].

These discrepancies suggested the presence of substantial noise in the 4D flow MRI acquisition process. To incorporate this information into the computational model, we utilized the average blood flow rate. However, it was crucial to account for this statistical uncertainty in the results. As a matter of fact, validation against *in vivo* data could not be treated as validation against a single "true value"; instead, it was essential for us to establish ranges in order to be able to compare against the distribution of measured kinetic energies. We addressed this by propagating the uncertainty into the kinetic energy within the ROI.

Another critical aspect pertains to the selection of model parameters. We determined that accurately choosing the Young’s modulus of the valve is paramount, as this parameter is patient-specific and significantly influences the results. Given its unknown value a priori, we conducted a calibration study to establish a range of variation for valve stiffness that yields outcomes in line with the *in vivo* data and their variation.

Given the inability to directly measure the valve’s Young modulus, lacking precise knowledge of calcification levels, and uniform severity of AS across all patients, we standardized the Young modulus value for the entire cohort. The chosen E_s value, calibrated from P1, facilitated compar-

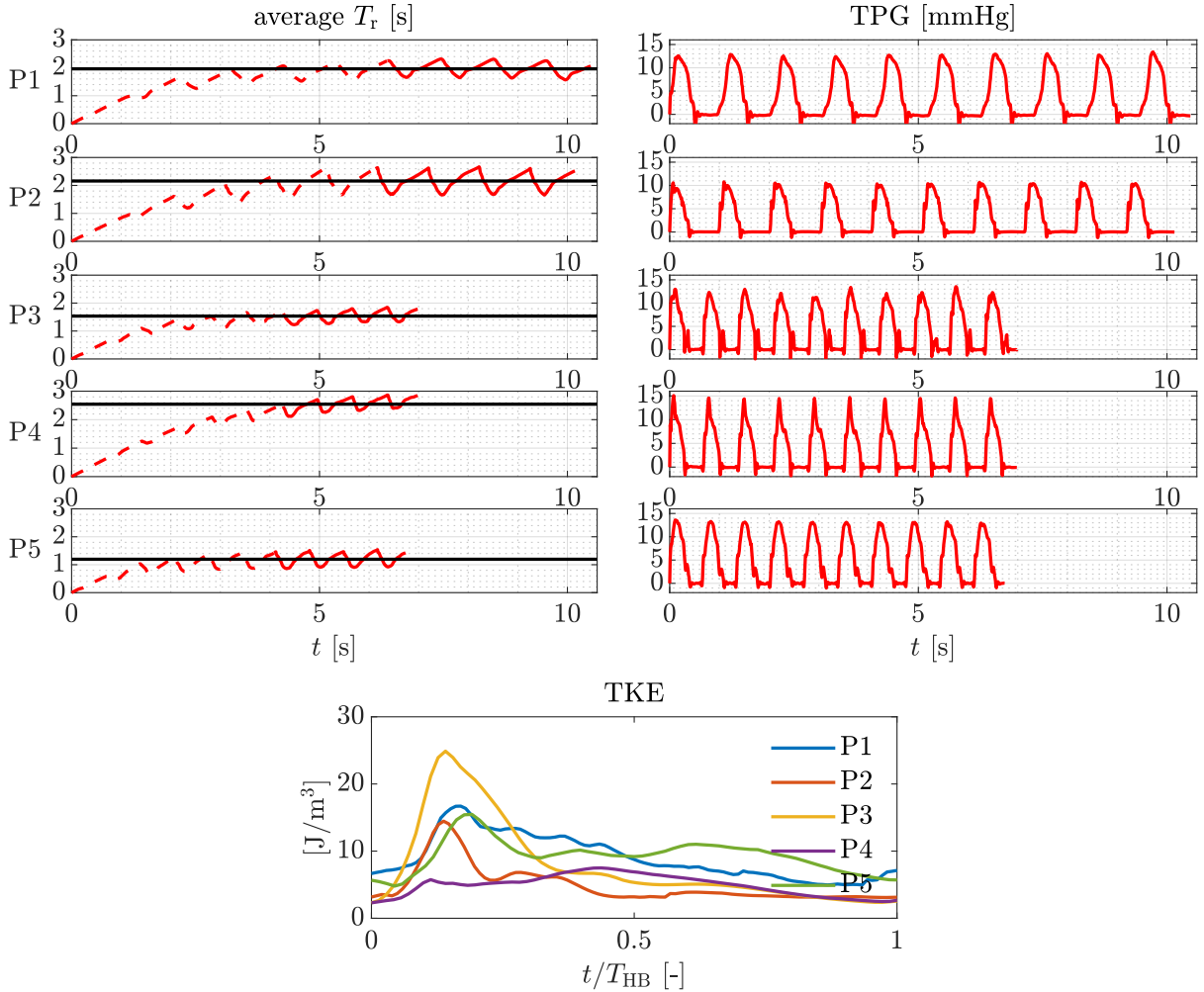


Figure 15: QoIs from FSI simulations for the five patients: on the left, average T_r for ten beats, in black, we report the average T_r by averaging the solution in the last four beats (solid red line) discarding the first six beats (dashed red line); on the right, the TPG for ten beats; on the bottom, the TKE on a representative cycle.

ative analysis across patients without overfitting the model. Moreover, this decision streamlined the pipeline, reducing computational overhead.

Validation of MKE reveals high accuracy for patient P1, with a relative error of 2.5% in terms of peak kinetic energy. However, for the remaining patients, all MKE values fall within the range of uncertainties, except for patient P2 and P5, where the FSI simulation underestimates the *in vivo* data. This underscores the significance of careful model parameter selection. Despite the calibration process being conducted on a single patient to establish a range of valve stiffness variation, the majority of other patients' results still fall within our range of uncertainties.

Regarding the validation of blood flow patterns, we observed that, overall, the FSI model realistically reproduces the patterns observed in the 4D flow MRI data. This includes the formation of a strong jet through the AV leaflets that impinges on the aortic wall. However, in the case of patient P3, we noted a distinct pattern compared to the other patients: the jet impinged on the opposite side of the wall. Our computational model failed to capture this variation. We attribute

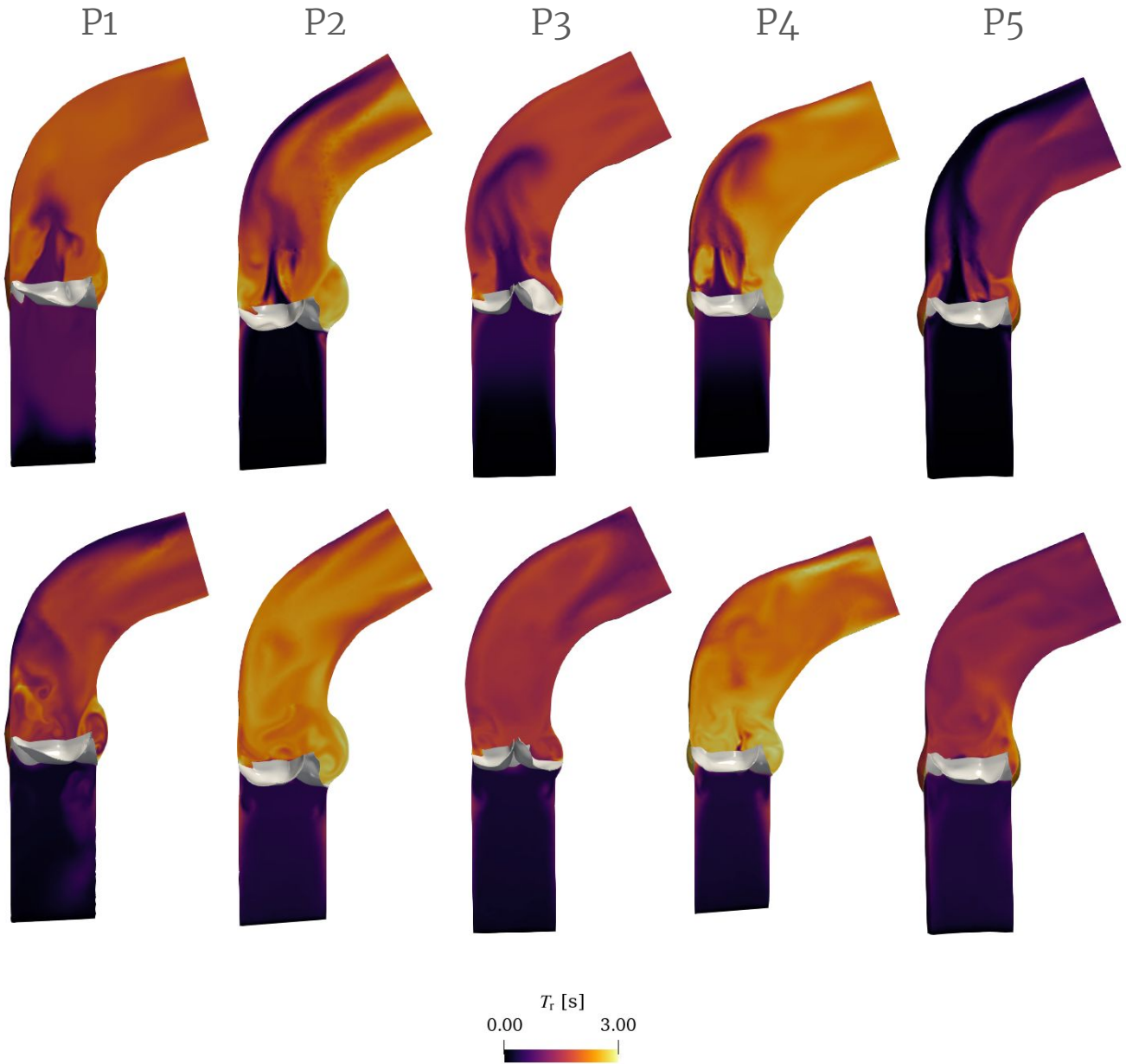


Figure 16: Residence time T_r for the five patients from FSI simulations for the five patients: on the top, systole; on the bottom, diastole. Result computed on the last heartbeat.

this discrepancy to the usage of the valve geometry from P1, adapted for the entire cohort, and potential differences in valve calcification among patients. Calcification could significantly alter the dynamics of AV opening, such as by blocking a specific leaflet. This underscores the importance of incorporating additional patient-specific features, such as valve geometry and calcification, into the computational model.

A comparison of the AVA highlighted how the FSI results were much more aligned with the measurements obtained from CT imaging compared to standard AVA measurements through echocardiography. This emphasized how standard methods of AVA measurement, based on the continuity equation, could produce results inconsistent with CT acquisitions and *in silico* technologies. This discrepancy mainly stemmed from the numerous assumptions made to compute AVA using the continuity method and the noise and uncertainty associated with the measured quantities used in its computation, which could significantly impact the final AVA result.

In attempting to validate shear stress quantities, we encountered greater challenges. Both computational and *in vivo* results exhibited similar profiles of both SSS and WSS, in terms of spatial distribution and transients. However, discrepancies in magnitudes often arose. The estimation of shear stresses is known to be limited by the relatively low spatial resolution of 4D flow MRI [78]. Additionally, we observed very large and unrealistic velocity values at the aorta boundary in the 4D flow data, on the order of 1500 mm s^{-1} . Consequently, while similar patterns may emerge, the reliability of 4D flow MRI data to this extent is questionable. Moreover, we speculate that incorporating the compliance of the wall into our model (using an FSI model for blood-wall interaction) would likely result in even smaller WSS values, as supported by recent studies [79]. Therefore, even by enriching our computational model with additional features such as aortic compliance, the WSS results would likely still not align well with those from 4D flow acquisition.

In a similar way, our comparison of turbulence quantities revealed that the computational model qualitatively reproduces the vorticity distribution in the aorta. However, when integrating this quantity to derive blood enstrophy, the FSI consistently underestimates the 4D flow MRI. We argue this discrepancy might be attributed to the reliability of 4D flow MRI data to accurately estimate velocity gradients.

Finally, we showed how the FSI simulations allow to compute additional QoIs often difficult to acquire with *in vivo* measurements, therefore enlarging the set of metrics and information extracted from medical imaging. This includes residence time, TPG and TKE.

5 Limitations and further developments

From a computational modeling perspective, it would be insightful to explore the impact of aortic compliance by incorporating the interaction between blood and the vessel wall, potentially through an Arbitrary Lagrangian Eulerian approach. It can be expected for compliance to affect blood velocity and WSS, potentially resulting in lower values of the latter [79]. In addition, a potential improvement would consist on using a more realistic pressure boundary condition on the outlet section, for instance with an *in vivo* pressure wave or a Windkessel model.

We utilized a Neo-Hookean constitutive law to model the AV, while anisotropic laws with a fiber description may be more appropriate [80]. However, it is important to note that this choice becomes particularly relevant if validation of valve motion itself is feasible. In this study, our focus was primarily on validating blood dynamics downstream of the valve. In addition, a possible improvement is to model the AV including calcification, for instance using a material model with a higher rigidity.

We used the same valve geometry for all the patients, whereas using the patient-specific valve – ideally directly from *in vivo* measurements – would potentially affect the results, especially in terms of flow patterns. However, while using the same valve model undoubtedly involves a compromise in terms of accuracy, it strategically balances precision against the preprocessing costs, aligning with the broader objective of our study, and is also in line with other computational studies on this topic [16, 81]. Furthermore, our calibration study of the Young modulus was limited to the first patient, and we applied the same valve model to the entire cohort. This approach may introduce biases and influence the outcomes of our results. Further investigations with a broader calibration study and patient-specific valve modeling could provide more robust insights.

Another limitation consists of the coarse resolution of the 4D flow MRI data: a finer resolution would allow us to carry on a more fair comparison between *in silico* results and *in vivo* measurements, especially in terms of vorticity. Additionally, signal loss near the valve during the acquisition process compromised the accuracy of the 4D flow MRI velocity acquisition in that region [76].

6 Conclusions

In this paper, we presented a comprehensive study aimed at validating blood flow downstream of the AV for five patients with AS using FSI models, with validation conducted against 4D flow MRI data.

We introduced a complete pipeline that incorporates various types of *in vivo* data (4D flow MRI and CT), *in vitro* data, and FSI computational modeling. This approach enabled the development of patient-specific FSI models for the interaction between the AV and aorta. Our computational model utilizes state-of-the-art IB-FSI methods within a HPC framework.

By utilizing flow rate data computed from 4D flow, we established ranges of variation for kinetic energy within an ROI downstream of the AV. The computational model consistently demonstrated the ability to accurately describe flow patterns and kinetic energy for most patients. Furthermore, our computational results yielded AVA values consistent with those computed using 4D flow MRI. Notably, both sets of results significantly differed from echocardiography measurements of AVA via the continuity equation.

Additionally, the computation of supplementary quantities derived from phase-averaged velocities, such as shear stresses and vorticity, revealed that while the model accurately captured similar patterns and transients as observed *in vivo*, there were often discrepancies in the values obtained. These discrepancies were attributed to a combination of low resolution and large, unrealistic velocities at the boundary of the aorta characterizing the 4D flow MRI data.

To summarize, this investigation underscores the efficacy of FSI models in faithfully replicating *in vivo* dynamics, while identifying the accurate reproduction of crucial indicators within specific ranges of uncertainties. Furthermore, we demonstrated how FSI enables the computation of supplementary biomechanical parameters, thereby enriching the insights obtainable from medical imaging. In addition, this study illustrates how *in silico* models can serve as a valuable cross-check to reduce noise and erratic behaviour in *in vivo* data.

Acknowledgements

This project was funded by the European Union - EIC Project No 190134524: “ELEM Virtual Heart Populations for Supercomputers” (ELVIS). Views and opinions expressed are, however, those

of the authors only and do not necessarily reflect those of the European Union or EISMEA. Neither the European Union nor the granting authority can be held responsible for them.

References

- [1] J. S. Aluru, A. Barsouk, K. Saginala, P. Rawla, A. Barsouk, Valvular heart disease epidemiology, *Medical Sciences* 10 (2022) 32.
- [2] American Heart Association, Aortic stenosis overview, <https://www.heart.org/en/health-topics/heart-valve-problems-and-disease/heart-valve-problems-and-causes/problem-aortic-valve-stenosis>, 2024-01-08.
- [3] National Heart, Lung and Blood Institute, Transcatheter aortic valve replacement (tavr), <https://www.nhlbi.nih.gov/health/tavr>, 2024-01-22.
- [4] A. Cribier, H. Eltchaninoff, A. Bash, N. Borenstein, C. Tron, F. Bauer, G. Derumeaux, F. Anselme, F. Laborde, M. B. Leon, Percutaneous transcatheter implantation of an aortic valve prosthesis for calcific aortic stenosis: first human case description, *Circulation* 106 (2002) 3006–3008.
- [5] J. P. Fanning, D. G. Platts, D. L. Walters, J. F. Fraser, Transcatheter aortic valve implantation (tavi): valve design and evolution, *International journal of cardiology* 168 (2013) 1822–1831.
- [6] H. Baumgartner, J. Hung, J. Bermejo, J. B. Chambers, A. Evangelista, B. P. Griffin, B. Iung, C. M. Otto, P. A. Pellikka, M. Quiñones, Echocardiographic assessment of valve stenosis: EAE/ASE recommendations for clinical practice, *European Journal of Echocardiography* 10 (2009) 1–25.
- [7] C. M. Otto, A. S. Pearlman, K. A. Comess, R. P. Reamer, C. L. Janko, L. L. Huntsman, Determination of the stenotic aortic valve area in adults using doppler echocardiography, *journal of the American College of Cardiology* 7 (1986) 509–517.
- [8] W. A. Zoghbi, J. B. Chambers, J. G. Dumesnil, E. Foster, J. S. Gottdiener, P. A. Grayburn, B. K. Khandheria, R. A. Levine, G. R. Marx, F. A. Miller, et al., Recommendations for evaluation of prosthetic valves with echocardiography and doppler ultrasound: a report from the american society of echocardiography’s guidelines and standards committee and the task force on prosthetic valves, developed in conjunction with the american college of cardiology cardiovascular imaging committee, cardiac imaging committee of the american heart association, the european association of echocardiography, a registered branch of the european society of cardiology, the japanese society of echocardiography and the canadian society of echocardiography, endorsed by the american college of cardiology foundation, american heart association, european association of echocardiography, a registered branch of the european society of cardiology, the japanese society of echocardiography, and canadian society of echocardiography, *Journal of the American Society of Echocardiography* 22 (2009) 975–1014.
- [9] G. T. Archer, A. Elhawaz, N. Barker, B. Fidock, A. Rothman, R. Van Der Geest, R. Hose, N. Briffa, I. R. Hall, E. Grech, et al., Validation of four-dimensional flow cardiovascular magnetic resonance for aortic stenosis assessment, *Scientific reports* 10 (2020) 10569.

- [10] R. Manzo, F. Ilardi, D. Nappa, A. Mariani, D. Angellotti, M. Immobile Molaro, G. Sgherzi, D. S. Castiello, F. Simonetti, C. Santoro, et al., Echocardiographic evaluation of aortic stenosis: A comprehensive review, *Diagnostics* 13 (2023) 2527.
- [11] M. T. Ngo, C. I. Kim, J. Jung, G. H. Chung, D. H. Lee, H. S. Kwak, Four-dimensional flow magnetic resonance imaging for assessment of velocity magnitudes and flow patterns in the human carotid artery bifurcation: Comparison with computational fluid dynamics, *Diagnostics* 9 (2019) 223.
- [12] M.-A. Clavel, J. Malouf, D. Messika-Zeitoun, P. A. Araoz, H. I. Michelena, M. Enriquez-Sarano, Aortic valve area calculation in aortic stenosis by ct and doppler echocardiography, *Cardiovascular Imaging* 8 (2015) 248–257.
- [13] B. Velders, R. Groenwold, A. Kappetein, J. Braun, R. Klautz, M. Vriesendorp, Measurement error in echocardiographic assessment of aortic stenosis: an epidemiological consideration of research methodology and clinical practice, *European Heart Journal* 43 (2022) ehac544–2863.
- [14] H. G. Bahraseman, E. M. Languri, N. Yahyapourjalaly, D. M. Espino, Fluid-structure interaction modeling of aortic valve stenosis at different heart rates, *Acta of bioengineering and biomechanics* 18 (2016) 11–20.
- [15] C. Zhu, J.-H. Seo, R. Mittal, Computational modeling of aortic stenosis with a reduced degree-of-freedom fluid-structure interaction valve model, *Journal of Biomechanical Engineering* 144 (2022) 031012.
- [16] I. Fumagalli, R. Polidori, F. Renzi, L. Fusini, A. Quarteroni, G. Pontone, C. Vergara, Fluid-structure interaction analysis of transcatheter aortic valve implantation, *International Journal for Numerical Methods in Biomedical Engineering* (2023) e3704.
- [17] G. Luraghi, F. Migliavacca, A. García-González, C. Chiastra, A. Rossi, D. Cao, G. Stefanini, J. F. Rodriguez Matas, On the modeling of patient-specific transcatheter aortic valve replacement: a fluid–structure interaction approach, *Cardiovascular engineering and technology* 10 (2019) 437–455.
- [18] G. Luraghi, J. F. R. Matas, M. Beretta, N. Chiozzi, L. Iannetti, F. Migliavacca, The impact of calcification patterns in transcatheter aortic valve performance: a fluid-structure interaction analysis, *Computer Methods in Biomechanics and Biomedical Engineering* 24 (2020) 375–383.
- [19] R. P. Ghosh, G. Marom, M. Bianchi, K. D’souza, W. Zietak, D. Bluestein, Numerical evaluation of transcatheter aortic valve performance during heart beating and its post-deployment fluid–structure interaction analysis, *Biomechanics and modeling in mechanobiology* 19 (2020) 1725–1740.
- [20] A. A. Basri, M. Zuber, E. I. Basri, M. S. Zakaria, A. F. Aziz, M. Tamagawa, K. A. Ahmad, et al., Fluid structure interaction on paravalvular leakage of transcatheter aortic valve implantation related to aortic stenosis: A patient-specific case, *Computational and mathematical methods in medicine* 2020 (2020).
- [21] J. De Hart, F. Baaijens, G. Peters, P. Schreurs, A computational fluid-structure interaction analysis of a fiber-reinforced stentless aortic valve, *Journal of biomechanics* 36 (2003) 699–712.

- [22] D. Oks, S. Reza, M. Vázquez, G. Houzeaux, B. Kovarovic, C. Samaniego, D. Bluestein, Effect of sinotubular junction size on TAVR leaflet thrombosis: A fluid–structure interaction analysis, *Annals of Biomedical Engineering* (2023) 1–15.
- [23] D. Oks, G. Houzeaux, M. Vázquez, M. Neidlin, C. Samaniego, Effect of TAVR commissural alignment on coronary flow: A fluid-structure interaction analysis, *Computer Methods and Programs in Biomedicine* 242 (2023) 107818.
- [24] D. Oks, C. Samaniego, G. Houzeaux, C. Butakoff, M. Vázquez, Fluid–structure interaction analysis of eccentricity and leaflet rigidity on thrombosis biomarkers in bioprosthetic aortic valve replacements, *International Journal for Numerical Methods in Biomedical Engineering* 38 (2022) e3649.
- [25] D. M. McQueen, C. S. Peskin, E. L. Yellin, Fluid dynamics of the mitral valve: physiological aspects of a mathematical model, *American Journal of Physiology-Heart and Circulatory Physiology* 242 (1982) H1095–H1110.
- [26] M. Astorino, J.-F. Gerbeau, O. Pantz, K.-F. Traoré, Fluid–structure interaction and multi-body contact: application to aortic valves, *Computer Methods in Applied Mechanics and Engineering* 198 (2009) 3603–3612.
- [27] B. E. Griffith, Immersed boundary model of aortic heart valve dynamics with physiological driving and loading conditions, *International journal for numerical methods in biomedical engineering* 28 (2012) 317–345.
- [28] G. Marom, Numerical methods for fluid–structure interaction models of aortic valves, *Archives of Computational Methods in Engineering* 22 (2015) 595–620.
- [29] Y. Aboelkassem, D. Savic, S. G. Campbell, Mathematical modeling of aortic valve dynamics during systole, *Journal of theoretical biology* 365 (2015) 280–288.
- [30] V. Flamini, A. DeAnda, B. E. Griffith, Immersed boundary-finite element model of fluid–structure interaction in the aortic root, *Theoretical and computational fluid dynamics* 30 (2016) 139–164.
- [31] M. Fedele, E. Faggiano, L. Dedè, A. Quarteroni, A patient-specific aortic valve model based on moving resistive immersed implicit surfaces, *Biomechanics and modeling in mechanobiology* 16 (2017) 1779–1803.
- [32] J. H. Spühler, J. Jansson, N. Jansson, J. Hoffman, 3d fluid-structure interaction simulation of aortic valves using a unified continuum ale fem model, *Frontiers in physiology* 9 (2018) 363.
- [33] M. C. Wu, H. M. Muchowski, E. L. Johnson, M. R. Rajanna, M.-C. Hsu, Immersogeometric fluid–structure interaction modeling and simulation of transcatheter aortic valve replacement, *Computer Methods in Applied Mechanics and Engineering* 357 (2019) 112556.
- [34] I. Fumagalli, M. Fedele, C. Vergara, S. Ippolito, F. Nicolò, C. Antona, R. Scrofani, A. Quarteroni, et al., An image-based computational hemodynamics study of the systolic anterior motion of the mitral valve, *Computers in biology and medicine* 123 (2020) 103922.

- [35] A. Zingaro, M. Bucelli, I. Fumagalli, L. Dede', A. Quarteroni, Modeling isovolumetric phases in cardiac flows by an augmented resistive immersed implicit surface method, *International Journal for Numerical Methods in Biomedical Engineering* (2022) e3767.
- [36] L. Bennati, V. Giambruno, F. Renzi, V. Di Nicola, C. Maffei, G. Puppini, G. B. Luciani, C. Vergara, Turbulent blood dynamics in the left heart in the presence of mitral regurgitation: a computational study based on multi-series cine-mri, *Biomechanics and Modeling in Mechanobiology* 22 (2023) 1829–1846.
- [37] A. Zingaro, M. Bucelli, R. Piersanti, F. Regazzoni, L. Dede', A. Quarteroni, An electromechanics-driven fluid dynamics model for the simulation of the whole human heart, *Journal of Computational Physics* (2024) 112885.
- [38] A. G. Kuchumov, A. Makashova, S. Vladimirov, V. Borodin, A. Dokuchaeva, Fluid–structure interaction aortic valve surgery simulation: A review, *Fluids* 8 (2023) 295.
- [39] U.S. Department of Health and Human Services, Food and Drug Administration, Center for Devices and Radiological Health, Assessing the Credibility of Computational Modeling and Simulation in Medical Device Submissions, Technical Report, 2023.
- [40] D. Gallo, U. Gülan, A. Di Stefano, R. Ponzini, B. Lüthi, M. Holzner, U. Morbiducci, Analysis of thoracic aorta hemodynamics using 3d particle tracking velocimetry and computational fluid dynamics, *Journal of biomechanics* 47 (2014) 3149–3155.
- [41] S. Toggweiler, B. De Boeck, O. Karakas, U. Gülan, Turbulent kinetic energy loss and shear stresses before and after transcatheter aortic valve replacement, *Case Reports* 4 (2022) 318–320.
- [42] U. Gülan, V. A. Rossi, A. Gotschy, A. M. Saguner, R. Manka, C. B. Brunckhorst, F. Duru, C. M. Schmied, D. Niederseer, A comparative study on the analysis of hemodynamics in the athlete's heart, *Scientific Reports* 12 (2022) 16666.
- [43] K. Dumont, J. Stijnen, J. Vierendeels, F. Van De Vosse, P. Verdonck, Validation of a fluid–structure interaction model of a heart valve using the dynamic mesh method in fluent, *Computer methods in biomechanics and biomedical engineering* 7 (2004) 139–146.
- [44] G. Luraghi, W. Wu, F. De Gaetano, J. F. R. Matas, G. D. Moggridge, M. Serrani, J. Stasiak, M. L. Costantino, F. Migliavacca, Evaluation of an aortic valve prosthesis: Fluid-structure interaction or structural simulation?, *Journal of biomechanics* 58 (2017) 45–51.
- [45] A. M. Tango, J. Salmonsmith, A. Ducci, G. Burriesci, Validation and extension of a fluid–structure interaction model of the healthy aortic valve, *Cardiovascular Engineering and Technology* 9 (2018) 739–751.
- [46] D. Sodhani, S. Reese, A. Aksenov, S. Soğancı, S. Jockenhövel, P. Mela, S. E. Stapleton, Fluid-structure interaction simulation of artificial textile reinforced aortic heart valve: Validation with an in-vitro test, *Journal of biomechanics* 78 (2018) 52–69.
- [47] F. Borowski, R. Ott, J. Oldenburg, S. Kaule, A. Öner, K.-P. Schmitz, M. Stiehm, Validation of a fluid structure interaction model for TAVR using particle image velocimetry, in: *Current Directions in Biomedical Engineering*, volume 8, De Gruyter, 2022, pp. 512–515.

- [48] C. S. Peskin, Flow patterns around heart valves: a numerical method, *Journal of computational physics* 10 (1972) 252–271.
- [49] R. Kikinis, S. D. Pieper, K. G. Vosburgh, 3d slicer: a platform for subject-specific image analysis, visualization, and clinical support, in: *Intraoperative imaging and image-guided therapy*, Springer, 2013, pp. 277–289.
- [50] Beta Simulation Solution, Ansa preprocessor. the advanced cae pre-processing software for complete model build up, <https://www.beta-cae.com/ansa.htm>, 2024-01-22.
- [51] U. Gülan, C. Binter, S. Kozerke, M. Holzner, Shear-scaling-based approach for irreversible energy loss estimation in stenotic aortic flow—an in vitro study, *Journal of biomechanics* 56 (2017) 89–96.
- [52] T. Zeugin, F. B. Coulter, U. Gülan, A. R. Studart, M. Holzner, In vitro investigation of the blood flow downstream of a 3d-printed aortic valve, *Scientific Reports* 14 (2024) 1572.
- [53] MicroPort, Severe aortic valve stenosis, <https://microport.com/patients/severe-aortic-valve-stenosis>, 2024-01-26.
- [54] P. D. Stein, H. N. Sabbah, Turbulent blood flow in the ascending aorta of humans with normal and diseased aortic valves., *Circulation research* 39 (1976) 58–65.
- [55] A. Vreman, An eddy-viscosity subgrid-scale model for turbulent shear flow: Algebraic theory and applications, *Physics of fluids* 16 (2004) 3670–3681.
- [56] A. Pal, K. Anupindi, Y. Delorme, N. Ghaisas, D. A. Shetty, S. H. Frankel, Large eddy simulation of transitional flow in an idealized stenotic blood vessel: evaluation of subgrid scale models, *Journal of biomechanical engineering* 136 (2014) 071009.
- [57] S. Katz, A. Caiazzo, B. Moreau, U. Wilbrandt, J. Brüning, L. Goubergrits, V. John, Impact of turbulence modeling on the simulation of blood flow in aortic coarctation, *International Journal for Numerical Methods in Biomedical Engineering* 39 (2023) e3695.
- [58] E. L. Manchester, S. Pirola, M. Y. Salmasi, D. P. O’Regan, T. Athanasiou, X. Y. Xu, Analysis of turbulence effects in a patient-specific aorta with aortic valve stenosis, *Cardiovascular engineering and technology* 12 (2021) 438–453.
- [59] T. Belytschko, W. K. Liu, B. Moran, K. Elkhodary, *Nonlinear finite elements for continua and structures*, John wiley & sons, 2014.
- [60] J. De Hart, G. Peters, P. Schreurs, F. Baaijens, A three-dimensional computational analysis of fluid–structure interaction in the aortic valve, *Journal of biomechanics* 36 (2003) 103–112.
- [61] O. Lehmkuhl, G. Houzeaux, H. Owen, G. Chrysokentis, I. Rodríguez, A low-dissipation finite element scheme for scale resolving simulations of turbulent flows, *Journal of Computational Physics* 390 (2019) 51–65.
- [62] M. Vázquez, G. Houzeaux, S. Koric, A. Artigues, J. Aguado-Sierra, R. Arís, D. Mira, H. Calmet, F. Cucchietti, H. Owen, et al., Alya: Multiphysics engineering simulation toward exascale, *Journal of computational science* 14 (2016) 15–27.

- [63] A. Santiago, J. Aguado-Sierra, M. Zavala-Aké, R. Doste-Beltran, S. Gómez, R. Arís, J. C. Casas, E. Casoni, M. Vázquez, Fully coupled fluid-electro-mechanical model of the human heart for supercomputers, *International journal for numerical methods in biomedical engineering* 34 (2018) e3140.
- [64] L. Törnqvist, P. Vartia, Y. O. Vartia, How should relative changes be measured?, *The American Statistician* 39 (1985) 43–46.
- [65] A. Zingaro, L. Dede', F. Menghini, A. Quarteroni, et al., Hemodynamics of the heart's left atrium based on a variational multiscale-les numerical method, *European Journal of Mechanics-B/Fluids* 89 (2021) 380–400.
- [66] R. Bonow, B. Carabello, A. De Leon, L. Edmunds Jr, B. Fedderly, M. Freed, W. Gaasch, C. McKay, R. Nishimura, P. O'Gara, et al., Acc/aha guidelines for the management of patients with valvular heart disease. executive summary. a report of the american college of cardiology/american heart association task force on practice guidelines (committee on management of patients with valvular heart disease), *The Journal of heart valve disease* 7 (1998) 672–707.
- [67] J. Zhang, Z. Chen, B. P. Griffith, Z. J. Wu, Computational characterization of flow and blood damage potential of the new maglev ch-vad pump versus the hvad and heartmate ii pumps, *The International journal of artificial organs* 43 (2020) 653–662.
- [68] K. D. Keele, Leonardo da vinci as physiologist, *Postgraduate medical journal* 28 (1952) 521.
- [69] F. Robicsek, Leonardo da vinci and the sinuses of valsalva, *The Annals of thoracic surgery* 52 (1991) 328–335.
- [70] C. Chnafa, S. Mendez, F. Nicoud, Image-based large-eddy simulation in a realistic left heart, *Computers & Fluids* 94 (2014) 173–187.
- [71] C. Otto, R. Nishimura, R. Bonow, B. Carabello, J. Erwin, F. Gentile, H. Jneid, E. Krieger, M. Mack, C. McLeod, et al., Acc/aha guideline for the management of patients with valvular heart disease: Executive summary: A report of the american college of cardiology/american heart association joint committee on clinical practice guidelines, *Circulation* 143 (2021) e35–e71.
- [72] H. Baumgartner, V. Falk, J. J. Bax, M. De Bonis, C. Hamm, P. J. Holm, B. Iung, P. Lancellotti, E. Lansac, D. Rodriguez, et al., 2017 ESC/EACTS guidelines for the management of valvular heart disease, *European heart journal* 38 (2017) 2739–2786.
- [73] L. Rossini, P. Martinez-Legazpi, V. Vu, L. Fernandez-Friera, C. P. Del Villar, S. Rodriguez-Lopez, Y. Benito, M.-G. Borja, D. Pastor-Escuredo, R. Yotti, et al., A clinical method for mapping and quantifying blood stasis in the left ventricle, *Journal of biomechanics* 49 (2016) 2152–2161.
- [74] H. Hatoum, J. Dollery, S. M. Lilly, J. Crestanello, L. P. Dasi, Impact of patient-specific morphologies on sinus flow stasis in transcatheter aortic valve replacement: an in vitro study, *The Journal of thoracic and cardiovascular surgery* 157 (2019) 540–549.

- [75] J. Huang, Y. Wang, L. Lin, Z. Li, Z. Shan, S. Zheng, Comparison of dynamic changes in aortic diameter during the cardiac cycle measured by computed tomography angiography and transthoracic echocardiography, *Journal of Vascular Surgery* 69 (2019) 1538–1544.
- [76] C. Binter, U. Gülan, M. Holzner, S. Kozerke, On the accuracy of viscous and turbulent loss quantification in stenotic aortic flow using phase-contrast mri, *Magnetic resonance in medicine* 76 (2016) 191–196.
- [77] V. Knobloch, C. Binter, U. Gülan, A. Sigfridsson, M. Holzner, B. Lüthi, S. Kozerke, Mapping mean and fluctuating velocities by bayesian multipoint mr velocity encoding-validation against 3d particle tracking velocimetry, *Magnetic resonance in medicine* 71 (2014) 1405–1415.
- [78] S. Petersson, P. Dyverfeldt, T. Ebbers, Assessment of the accuracy of mri wall shear stress estimation using numerical simulations, *Journal of Magnetic Resonance Imaging* 36 (2012) 128–138.
- [79] J. Liu, W. Yang, I. S. Lan, A. L. Marsden, Fluid-structure interaction modeling of blood flow in the pulmonary arteries using the unified continuum and variational multiscale formulation, *Mechanics research communications* 107 (2020) 103556.
- [80] L. Cai, R. Zhang, Y. Li, G. Zhu, X. Luo, H. Gao, The comparison of different constitutive laws and fiber architectures for the aortic valve on fluid–structure interaction simulation, *Frontiers in Physiology* 12 (2021) 682893.
- [81] M. Criseo, I. Fumagalli, A. Quarteroni, S. M. Marianeschi, C. Vergara, Computational haemodynamics for pulmonary valve replacement by means of a reduced fluid-structure interaction model, *MOX Report (preprint)* 01 (2024).

Acronyms

AS	Aortic Stenosis. 1–4, 8, 14, 21, 22, 26
AV	Aortic Valve. 1–6, 8–11, 13, 14, 19, 21–23, 25, 26
AVA	Aortic Valve Area. 2, 17, 25, 26
CFD	Computational Fluid Dynamics. 2
CMR	Cardiac Magnetic Resonance. 2
CT	Computed Tomography. 2–4, 17, 25, 26
FDA	Food and Drug Administration. 3
FE	Finite Element. 9, 10
FSI	Fluid Structure Interaction. 2–5, 9–11, 14, 17–26
GOA	Geometric Orifice Area. 17

HPC High Performance Computing. 10, 26

IB Immersed Boundary. 3, 7, 9, 10, 26

LES Large Eddy Simulation. 8

LIC Line Integral Convolution. 21

LVOT Left Ventricle Outflow Track. 2

MKE Mean Kinetic Energy. 11–14, 16, 17, 19, 21, 23

MRI Magnetic Resonance Imaging. 2–5, 7, 8, 10–12, 14–16, 18–23, 25, 26

PIV Particle Image Velocimetry. 2

QoIs Quantities of Interest. 2–4, 10, 14, 21, 23, 25

ROI Region of Interest. 10–15, 18, 19, 21, 22, 26

SAVR Surgical Aortic Valve Replacement. 2

SoV Sinus of Valsalva. 6, 22

SSS Scalar Shear Stress. 18, 19, 25

TAVR Transcatheter Aortic Valve Replacement. 2–4, 21

TKE Turbulent Kinetic Energy. 21, 23, 25

TPG Transvalvular Pressure Gradient. 2, 21, 23, 25

VVUQ Verification, Validation, and Uncertainty Quantification. 2

WSS Wall Shear Stress. 18, 19, 21, 25